Monte Carlo Study of a Geometrically Frustrated Rare Earth Compound: $SrGd_2O_4$

by

Emrul Hasan

A Thesis submitted to the Faculty of Graduate Studies of
The University of Manitoba
in partial fulfillment of the requirements for the Degree of

MASTER OF SCIENCE

Department of Physics and Astronomy
University of Manitoba
Winnipeg

TABLE OF CONTENTS

LIST OF FIGURES

LIST OF TABLES

ACKNOWLEDGMENTS

I would like to express my sincere gratitude to my supervisor, Dr. Byron Southern. His help, stimulating suggestions, understanding, encouragement and personal guidance helped me in the research and writing of this thesis. I would like to express my appreciation to my examining committee members, Dr. Johan van Lierop and Dr. Christopher Wiebe.

I would also like to thank Dr. K.S. Sharma, former Head of the Department of Physics and Astronomy, and the Departmental secretaries, Wanda Klassen, Susan Beshta, Robyn Beaulieu and Maiko Langelaar, Programmer Analyst, for their support.

This research has been supported and funded by the Natural Science and Engineering Research Council (NSERC) and the Graduate Enhancement of Tri-Council Stipends (GETS). An International Graduate Student Entrance Scholarship (IGSES) is gratefully acknowledged.

ABSTRACT

We study the low temperature magnetic phase transitions and phase diagram of one member of the lathanide family of frustrated compounds, $SrGd_2O_4$, using Monte Carlo simulation techniques. Frustrated magnetism is the study of competing interactions between the neighbouring spins. Frustration occurs when the lattice geometry of the system is such that, with antiferromagnetic interactions, the system is unable to find an unique ground state to minimize the energy of the system. Recently, frustration has been identified in a rare earth family of compounds with the formula $SrLn_2O_4$ where $Ln = Ho, Gd, Er, Dy, Tm$, and Yb. The two dimensional honeycomb structure of $SrLn_2O_4$ in the ab plane is connected by triangular chains running along the c direction, which leads to frustration. In this thesis we focus on one of these frustrated materials, $SrGd_2O_4$.

A detailed experimental study of two members of the $SrLn_2O_4$ family of compounds, $SrHo_2O_4$ and $SrGd_2O_4$, has recently been carried out by Young[1]. In her extensive studies, magnetic bulk properties are measured with both single crystal and powder samples. Both compounds have the same structure but their magnetic behaviour is quite different. $SrHo_2O_4$ exhibits complex crystal field effects and an Ising anisotropy at low temperatures. In contrast, in the ground state of $SrGd_2O_4$, the orbital angular momentum $L = 0$ which allows us to neglect the spin orbit coupling interaction and crystal field effects and study this material with only Heisenberg exchange and dipole interactions. For $SrGd_2O_4$, two magnetic phase transitions in zero applied field are identified at two different temperatures from both specific heat and magnetisation measurements. Measurements of the magnetisation in an applied

field also indicate two transitions at low temperatures. A complex phase diagram of $SrGd_2O_4$ was mapped out in the field-temperature ($H-T$) plane from magnetisation, susceptibility and specific heat measurements and several ordered phases were identified. However, the detailed nature of these phases remains unknown. Dipolar interactions are believed to play an important role.

We have used a model of classical Heisenberg spins to investigate the low temperature behaviour. We have studied the cases of pure exchange and pure dipole interactions as well as their combined effects. Our simulation results qualitatively agree with the experimental findings. In zero applied field, two phase transitions are identified at two different temperatures from the specific heat and magnetisation measurements as a function of temperature T. Measurements of these quantities as a function of an applied field H also indicate several transitions at low temperatures Finally, by collecting data from all measured thermodynamic quantities, a $H-T$ phase diagram is constructed. It reveals four separate regions of phases with unique magnetic ordering. We have identified the nature of the order in each of these phases.

Chapter 1

INTRODUCTION

Scientific discussions on magnetism are known to have taken place from about 625 BC to about 545 BC [2]. Although research on magnetism began in ancient times, the study of magnetic phenomena continues to the present day. Fundamental research on magnetism started broadly after Oersted's experiments [3]. His experiments proved the relationship between electric currents and magnetism. Steady electric currents produce magnetic fields on their own. Electric currents and the magnetic moments of the elementary particles are responsible for magnetic fields as well as for the magnetism in many materials. Depending on the electronic configuration of materials, the magnetic properties can be quite different.

Magnetic materials have been used in technology since their discovery. The first use of magnetic materials was in surgery in ancient India by the Indian surgeon Sushruta [4]. Modern technology is widely dependent on the use of magnetic materials, including transformers, electric motors, loudspeakers, sensors, tapes(audio and video), MRI scanners, floppy disks and hard disk media, and MRAM (magnetic random access memory). Their use in recording industries, storage devices and electronics industries are increasing day by day.

The diversity of magnetism studies include solar physics, geophysics, material science, nanotechnology and condensed matter physics to name a few. In condensed matter physics, studies of geometrically frustrated magnetism is a fertile area of research for physicists mainly because of the unusual magnetic properties at low temper-

ature. Geometrical frustration in materials arises when a material's lattice geometry is unable to minimise the energy of all interacting spins simultaneously [5]. In materials with complex geometrical structures, frustration depends on various factors such as the lattice geometry, the strength and the sign of the interactions between the magnetic dipole moments. The simplest example of such a system is a magnet with equilateral triangular geometry [6, 7]. Some other well-known examples of frustrated materials are based on tetrahedra [8, 9, 10], and kagome geometries[11, 12]. Originally, the concept of frustration comes from spin glasses [13, 14] in which a frozen glass-like magnetic state occurs. Various types of magnetic order are found in the materials depending on the temperature T and the applied field H. Geometrically frustrated magnetic systems often exhibit a degenerate manifold ground state [15]. Low temperature magnetic properties and phase transitions are quite unusual in frustrated magnetic materials and have motivated physicists to study this exciting area of physics.

In this work we are interested in the low temperature magnetic properties of the frustrated rare earth compound $SrGd_2O_4$. Our study is based on the experimental work of Olga Young, a former PhD student in the Department of Physics at University of Warwick, England [1]. In her PhD research she studied the low temperature magnetic properties such as magnetisation and its field derivative, specific heat, and susceptibility. A field-temperature ($H - T$) phase diagram of $SrGd_2O_4$ was presented based on these measured quantities [16]. However, her studies were unable to identify the magnetic ordering in the different phases. Our main objective is to study the $SrGd_2O_4$ compound and understand the low temperature properties such as magnetisation, specific heat, susceptibility, phase transitions and the $H - T$ phase diagram.

We employ a Monte Carlo simulation technique to model the frustrated system [17]. To calculate the desired quantities we use the heat bath Monte Carlo method and we utilize the high performance computer facilities available at Westgrid/Compute

Canada to speed up the calculations as well as to be able to simulate large system sizes.

The outline of the thesis is as follows. In chapter 2 we present a very brief introduction to magnetism. The concept of geometrical frustration and its consequences are discussed in this chapter. The origins of direct exchange and superexchange interactions are also discussed. Chapter 3 is devoted to a description of the structure of the rare earth family of compounds ($SrLn_2O_4$) and their low temperature experimental magnetic properties. The crystal structure and detailed magnetic properties of the compound $SrGd_2O_4$ are included in this chapter. In chapter 4, we introduce a model Hamiltonian to describe $SrGd_2O_4$ and we discuss the Monte Carlo simulation technique that we use to study its properties. In chapter 5 we present our results from the simulations and compare with the experimental measurements. Chapter 6 provides a summary and conclusions.

Chapter 2

MAGNETISM AND MAGNETIC INTERACTIONS

In this chapter we discuss the origins of magnetism in materials and the consequences of geometrical frustration.

2.1 Magnetic Moments

The magnetic moment is a fundamental property of magnetism[18]. In classical electromagnetism, magnetic moments can be described in terms of current loops. If an electron moves with current I around an oriented loop of area $|\mathbf{dS}|$(see figure 2.1) then the magnetic dipole moment can be defined as

$$d\vec{\mu} = I d\vec{S} \tag{2.1}$$

and has units Am^2. The direction of the vector $d\vec{S}$ is perpendicular to the loop and is determined by the direction of the current around the loop using the right hand rule. Since the direction of the magnetic moment $\mathrm{d}\vec{\mu}$ is perpendicular to the plane of the current loop, the magnetic moment will be pointing either parallel or antiparallel to the angular momentum associated with revolving charge. The total magnetic moment $\vec{\mu}$ of the loop can be calculated by integrating over the area of the loop

$$\vec{\mu} = \int d\vec{\mu} = I \int d\vec{S} \tag{2.2}$$

Since the electrons in a current loop have mass m_e, the magnetic moment can be related to angular momentum. In atoms, the magnetic moment $\vec{\mu}$ associated with revolving electron lies along the same direction as the angular momentum. The

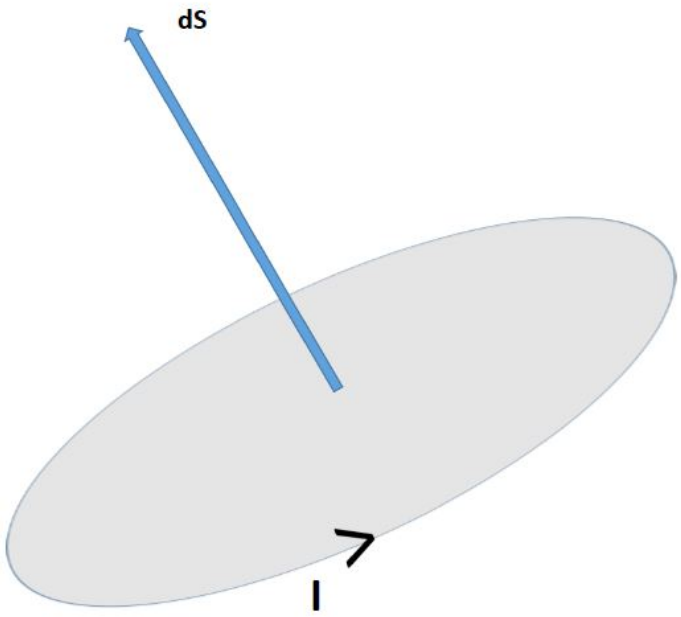

Figure 2.1: Magnetic moment produced by current carrying loop of infinitesimal area dS.

magnetic moment and angular momentum are related as

$$\vec{\mu} = \gamma \vec{L} \tag{2.3}$$

where $\gamma = -\frac{|e|}{2m_e}$ is called gyromagnetic ratio. The convention is that γ is negative for negatively charged particles. The magnetic moment can also be expressed in terms of the Bohr magneton

$$\mu_B = \frac{|e|\hbar}{2m_e} \tag{2.4}$$

which has the value $9.27 \times 10^{-24} Am^2$. Hence

$$\vec{\mu} = -\mu_B \vec{L}/\hbar \tag{2.5}$$

The magnetic moment of an electron has two contributions: orbital and spin. The electronic angular momentum associated with the motion of electron around nucleus is known as orbital angular momentum. The orbital angular momentum depends on the electronic state occupied by the electron with quantum numbers ℓ and m_ℓ where $\ell = 0, 1, 2, ...$ and $m_\ell = -\ell, -\ell+1, ...\ell-1, \ell$ since angular momentum is quantized. The electronic orbitals are eigenstates of the angular momentum operator L^2 with the eigenvalue $\ell(\ell+1)\hbar^2$. The z component of the angular momentum L_z has eigenvalue $m_\ell\hbar$ and the magnitude of angular momentum is taken to be $\sqrt{\ell(\ell+1)}\hbar$. Similarly the magnetic moment operators μ^2 and μ_z have the eigenvalues $\ell(\ell+1)\mu_B^2$ and $m_\ell\mu_B$ respectively. In addition to orbital angular momentum, an electron also possesses intrinsic angular momentum, called spin $\vec{S}$, which is characterised by the quantum numbers s and m_s. For a single electron s takes the value $\frac{1}{2}$ and the eigenvalue of the z component is $m_s = \pm\frac{1}{2}\hbar$. The eigenvalue of the operator S^2 is $s(s+1)\hbar^2$ and the magnitude of the spin is taken to be $\frac{\sqrt{3}\hbar}{2}$.

The corresponding spin magnetic moment along the z direction is $g_e\mu_B m_s$ where the g_e factor for an electron has the approximate value $g_e \sim 2$ and is due to a relativistic effect. Hence the total angular momentum of an electron is $\vec{J} = \vec{L} + \vec{S}$ but the total magnetic moment is $\vec{\mu} = -\frac{\mu_B}{\hbar}(\vec{L} + 2\vec{S})$.

2.2 Angular Momentum Coupling

We discussed orbital and spin angular momentum separately in the above section. However, in magnetic atoms with many electrons, the individual electronic contributions are combined to calculate the total orbital $\vec{L}$ and spin $\vec{S}$ angular momenta of the atom. These spin and orbital angular momenta couple due to the spin-orbit interaction $\lambda\vec{L}\cdot\vec{S}$. The quantities L^2, L_z, S^2, S_z are no longer separately conserved. A new set J^2, J_z, L^2, S^2 are conserved and the states can be labelled in terms of j, m_j, ℓ, s. The quantum number j can take the values $|\ell - s|, ...(\ell + s - 1), (\ell + s)$ and m_j can take the $2j + 1$ values $-j, -j + 1, ..., j$.

As noted above the total magnetic moment is related to $\vec{L} + 2\vec{S}$ and can be expressed in terms of $\vec{J}$ as follows

$$\vec{\mu} = -g_j \mu_B \vec{J}/\hbar \tag{2.6}$$

where g_j is the Landé g-factor and is given by

$$g_j = 1 + \frac{j(j+1) + s(s+1) - l(l+1)}{2j(j+1)} \tag{2.7}$$

Note that $g_j = 1$ for pure orbital motion ($s = 0$) and $g_j = 2$ for the spin only case ($\ell = 0$).

2.2.1 Hund's Rules

In a many electron atom, there are two methods of forming the total angular momentum [19]. These are referred to as Russell-Saunders coupling and $j - j$ coupling. In the case where the spin-orbit coupling is weak, Russell-Saunders is used to first form a total $\vec{L} = \sum_i \vec{\ell_i}$ and total $\vec{S} = \sum_i \vec{s_i}$ for the atom and then combine these to form a total $\vec{J}$. When the spin-orbit coupling is strong, a total $\vec{j_i}$ is formed for each electron first and then these are used to form the total $\vec{J}$. In the case of the lathanides, we use

Russell-Saunders coupling and Hund's rules to form the total angular momentum of the atom.

These rules are as follows:

1. electron spins are aligned to form the largest possible value of S consistent with the Pauli principle.

2. in a given subshell, the states with largest m_ℓ are filled first.

3. the total $J = L - S$ for less than half-filled shells and $J = L + S$ for more than half-filled shells.

2.3 Magnetic Moments and Applied Magnetic Fields

The magnetic induction $\vec{B}$ and the magnetic field strength $\vec{H}$ are related in vacuum by the following linear relation

$$\vec{B} = \mu_0 \vec{H} \tag{2.8}$$

where permeability of free space $\mu_0 = 4\pi \times 10^{-7} N A^{-2}$. It is important to note that there is a subtle difference between these two fields. The induction $\vec{B}$ is measured in units of Tesla(T) whereas the magnetic field strength $\vec{H}$ is measured in units of Am^{-1} and $1T = \frac{N}{A.m} = \frac{J}{A.m^2}$.

Magnetic moments per unit volume are known as the magnetisation $\vec{M}$. The relation between magnetisation and fields is given by

$$\vec{B} = \mu_0(\vec{H} + \vec{M}) \tag{2.9}$$

In case of linear materials the magnetic field strength $\vec{H}$ and the magnetisation $\vec{M}$ are related by

$$\vec{M} = \chi \vec{H} \tag{2.10}$$

where χ is the magnetic susceptibility, a dimensionless quantity, defined as the ratio of the magnetic moment induced by the applied field per unit volume to the field strength. Hence equation (2.9) can be written as

$$\vec{B} = \mu_0(1+\chi)\vec{H} = \mu_0\mu_r\vec{H} \tag{2.11}$$

where $\mu_r = 1 + \chi$ is called the relative permeability of the material.

The energy E of a magnetic moment $\vec{\mu}$ in a magnetic field $\vec{B}$ is given by

$$E = -\vec{\mu}.\vec{B} \tag{2.12}$$

and depends on the alignment of $\vec{\mu}$ with respect to $\vec{B}$.

2.4 Magnetic Order

In materials with nonzero magnetic moments on the atoms, there are several different types of arrangements of the directions of the moments. At high temperatures, thermal disorder leads to a random arrangement of the magnetic moment directions called paramagnetism. In this case, there is no net magnetic moment but the moments can be aligned with the application of a magnetic field. At low temperatures, the magnetic moments can order spontaneously in the absence of an external field. The ordering is due to interactions between the magnetic moments on the individual atoms called exchange interactions. These interactions are a quantum mechanical effect due to the indistinuishability of identical particles and the fact that electrons obey Fermi-Dirac statistics. The interactions can lead to ordered phases called ferromagnetism, anti-ferromagnetism, and ferrimagnetism as illustrated in Fig 2.2.

2.4.1 Direct Exchange

The electrons in a material can interact in many ways including exchange interactions, dipole-dipole interactions and Coulomb interactions[20]. The exchange interaction

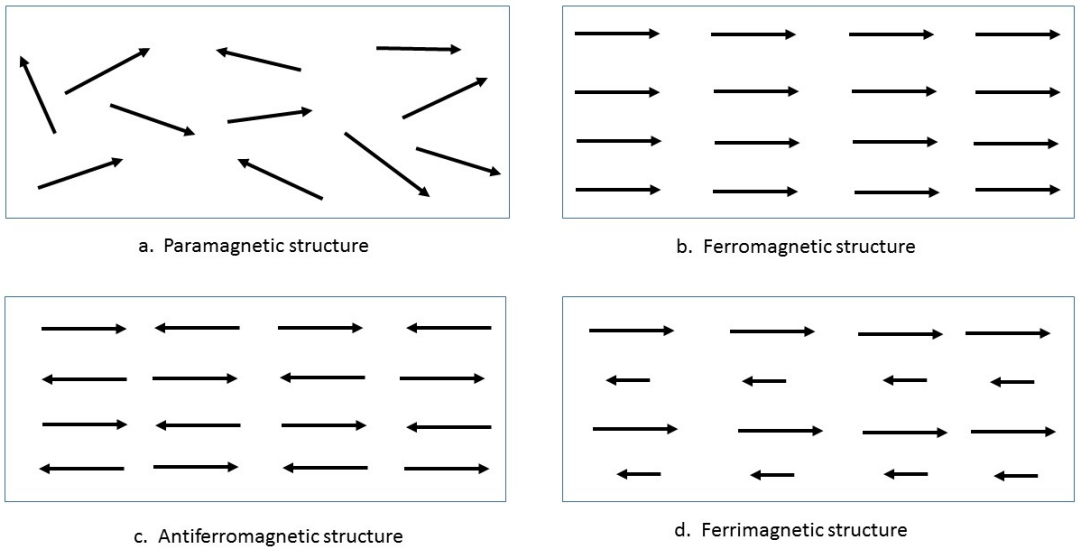

Figure 2.2: Various types of magnetic order a) paramagnetism, b) ferromagnetism, c) antiferromagnetism, and d) ferrimagnetism.

coupling is quantum mechanical in origin and occurs via electrons shared by atoms whereas the dipolar and Coulomb interactions are long-ranged between magnetic moments and electric charges respectively.

The exchange interaction can be understood by considering a simple hydrogen molecule, with two electrons and two protons interacting via the Coloumb interaction. The Hamiltonian of the system is

$$\mathcal{H} = \frac{p_1^2 + p_2^2}{2m} + e^2\left(\frac{1}{r_{ij}} + \frac{1}{r_{12}} - \frac{1}{r_{i1}} - \frac{1}{r_{i2}} - \frac{1}{r_{j1}} - \frac{1}{r_{j2}}\right) \tag{2.13}$$

where e and m are the charge and mass of the electrons respectively. The indices 1 and 2 label the electrons whereas i and j label the two protons. First term represents the kinetic energy of the two electrons with momenta p_1 and p_2. The $r_{\alpha\beta}$ are the distances between the various pairs of particles and the protons are at a fixed distance r_{ij}. The total wave function of the two electrons is the product of a spin and spatial part. The

total wave function ψ is therefore

$$\psi(r_1\sigma_1, r_2\sigma_2) = \Phi(r_1, r_2)\chi(\sigma_1, \sigma_2) \tag{2.14}$$

where the spin coordinates σ_1 and σ_2 are the projections of spin along a given axis. $\Phi(r_1, r_2)$ is the spatial part of the wave function with the space co-ordinates. According to the Pauli principle, the total wave function must be anti-symmetric if all the coordinates of the two electrons are interchanged. The spin function χ is symmetric when the total spin $S = 1$ and anti-symmetric when $S = 0$. Therefore a symmetric spatial wave function must be combined with an anti-symmetric spin wavefunction and vice versa as follows

$$\begin{aligned} \psi(r_1\sigma_1, r_2\sigma_2) &= \Phi_S(r_1, r_2)\chi_A(\sigma_1, \sigma_2), (S = 0) \\ &= \Phi_A(r_1, r_2)\chi_S(\sigma_1, \sigma_2), (S = 1) \end{aligned} \tag{2.15}$$

where S and A denote symmetric and antisymmetric wave functions respectively. The symmetric and antisymmetric spatial functions can be written as

$$\begin{aligned} \Phi_S(r_1, r_2) &= \frac{1}{\sqrt{2(1+c^2)}}(\Phi(r_{i1})\Phi(r_{j2}) + \Phi(r_{i2})\Phi(r_{j1})) \\ \Phi_A(r_1, r_2) &= \frac{1}{\sqrt{2(1-c^2)}}(\Phi(r_{i1})\Phi(r_{j2}) - \Phi(r_{i2})\Phi(r_{j1})) \end{aligned} \tag{2.16}$$

where the normalization constant

$$c = \int\int\int \Phi(r(i1))\Phi(r(j1))d^3r_1 = \int\int\int \Phi(r(i2))\Phi(r(j2))d^3r_2 \tag{2.17}$$

is the overlap of the electron wave functions centered on the two protons.

The triplet ($S = 1$) and the singlet ($S = 0$) states have different energies given by

$$E_{\uparrow\uparrow} = \frac{P(r_{ij}) - Q(r_{ij})}{\sqrt{1-c^2}} \quad (S = 1) \tag{2.18}$$

$$E_{\uparrow\downarrow} = \frac{P(r_{ij}) + Q(r_{ij})}{\sqrt{1-c^2}} \quad (S=0)$$

where P and Q are the electrostatic terms which depend on the separation of two protons. The total Hamiltonian can be written as

$$\mathcal{H} = -J(r_{ij})\vec{S}_1 \cdot \vec{S}_2 + E(r_{ij}) \tag{2.19}$$

where the first term depends on the relative orientation of the spins and the second term is independent of the spin orientation. $J(r_{ij})$ is the exchange integral and is given by

$$J(r_{ij}) = E_{\uparrow\uparrow} - E_{\uparrow\downarrow} \tag{2.20}$$

and depends on the energy difference between the triplet and singlet configurations. Apart from a constant, the energy of the spin system interacting through direct exchange is[21, 22]

$$\mathcal{H} = -\sum_{i<j} J(r_{ij})\vec{S}_i.\vec{S}_j \tag{2.21}$$

where $\vec{S}_i$ and $\vec{S}_j$ are the spins at lattice sites i and j. If $J(r_{ij}) > 0$, the two spins prefer to be aligned parallel and the material is ferromagnetic. If $J(r_{ij}) < 0$, the spins prefer to be anti-parallel and the material can be an antiferromagnet. However, as we shall discuss below, negative exchange interactions often lead to frustration and the magnetic order is more complex.

2.4.2 Superexchange

The idea of superexchange was first proposed by the Dutch Physicist Hendrik Kramers in 1934 when he noticed that MnO is antiferromagnetic but there was little direct overlap of the wavefunctions on neighbouring atoms[23]. He found that when Mn^{2+} ions are connected through an intervening non-magnetic O^{2-} ion, the interactions

between the Mn^{2+} are antiferromagnetic. This interaction is a strong interaction compared to direct exchange. In direct exchange the strength of interaction rapidly decreases with increasing the distance between the atoms. Superexchange is usually found in transition metal oxides such as MnO and CoO. In 1959 Anderson[24] considered a molecular orbital formed by the mixture of the localized 3d orbitals and orbitals of the intervening negative ion. The bonding orbital is mainly occupied by the negative ion, while the anti bonding orbital is partially occupied by 3d electrons, leading to the magnetism of the system. Thus the wave function of localized d spins extends over the neighbouring negative ion. There is a probability of transferring from one 3d orbital of the magnetic ion to the neighbouring 3d orbitals, leading to an exchange interaction.

A more sophisticated system of semi-empirical rules was developed by Goodenough and Kanamori in the 1950s[25, 26, 27]. In their rules they described the important features of taking into account the occupation of the various d levels. The main features are actually explained in terms of so called Goodenough- Kanamori-Anderson rules. According to the rules 180 degree cation- anion- cation interaction is strongly antiferromagnetic when two magnetic ions have partially filled d shells. On the other hand 90 degree interaction is ferromagnetic and much weaker.

2.5 Paramagnetism

Paramagnetism corresponds to positive susceptibilities in the presence of an external magnetic field. At high field and zero temperature the magnetic moments are aligned along the direction of the field. The magnetic moment of an atom is proportional to the total angular momentum $\vec{J}$ of the atom. The partition function for an atom with total angular momentum quantum number j in a magnetic field is

$$Z = \sum_{m_j=-j}^{j} exp(m_j g_j \mu_B \mu_0 H/k_B T) \tag{2.22}$$

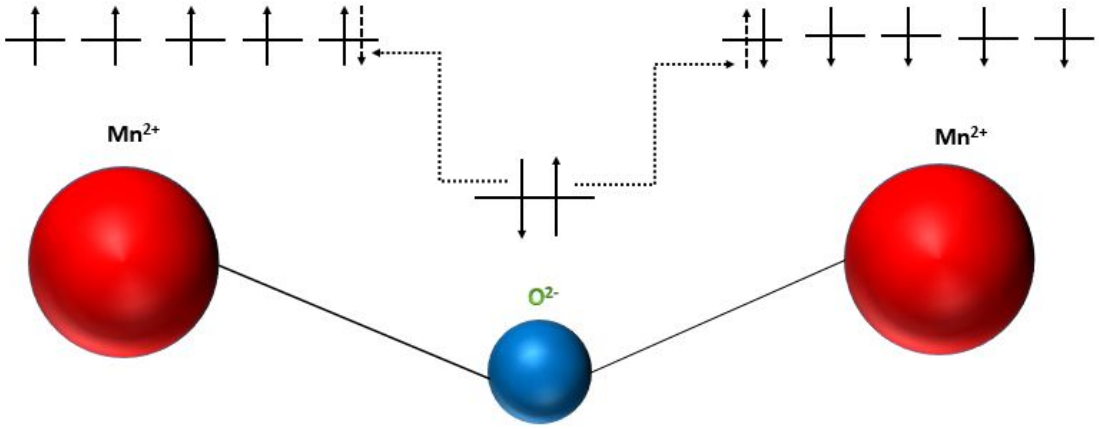

Figure 2.3: A superexchange interaction, where the magnetic Mn^{2+} ions interact antiferromagnetically through non-magnetic O^{2-} ion.

The Helmholtz free energy is $F = -k_BTlnZ$ and the magnetisation is given by $k_BT\frac{\partial lnZ}{\partial H}$ and yields

$$M = M_sB_j(y) \tag{2.23}$$

where $y = g_j\mu_Bj\mu_0H/k_BT$, $M_s = g_j\mu_Bj$ is the saturation magnetisation and $B_j(y)$ is the Brillouin function which has the form

$$B_j(y) = \frac{2j+1}{2j}coth(\frac{2j+1}{2j}y) - \frac{1}{2j}coth\frac{y}{2j} \tag{2.24}$$

In case of $j = \infty$ and $j = \frac{1}{2}$, the Brillouin function reduces to the classical Langevin function $\mathcal{L}(y) = coth(y) - \frac{1}{y}$ and the $tanh(y)$ function respectively. At low magnetic field and high temperature (i.e. small y), the Brillouin function can be written as $B_j(y) \approx (j+1)y/3j + \mathcal{O}(y^3)$. Therefore, the susceptibility in this limit is given by

$$\chi = \frac{M}{H} = \frac{\mu_0 \mu_{eff}^2}{3k_B T} \tag{2.25}$$

where

$$\mu_{eff} = g_j \mu_B \sqrt{j(j+1)} \tag{2.26}$$

is the effective moment.

In the above, no interactions between the atoms are taken into account. In the presence of exchange, the field H should include the exchange field $\sum_j J_{ij} S_j$ due to the neighbours. In this case the magnetic susceptibility for the interacting system can be written as

$$\chi = \frac{C}{T - \theta_{CW}} \tag{2.27}$$

where $C = \mu_0 g_j^2 \mu_B^2 j(j+1)/3k_B$ is the Curie constant and $\theta_{CW} = \frac{j(j+1)\sum_j J_{ij}}{3k_B}$ is the Curie Weiss temperature. A plot of the inverse susceptibility versus temperature will vanish at θ_{CW} is shown in Fig.2.4. For a paramagnet with no interactions it vanishes at T=0 but, depending on the signs of the exchange parameters J_{ij}, it vanishes at a positive (ferromagnet) or negative temperature (antiferromagnet).

2.6 Magnetic Dipole Interactions

Atomic spins can be considered as a tiny magnetic dipole with one end of the spin as the north pole and the other end as the south pole. The dipole interaction between the magnetic dipole moments μ_i and μ_j is defined by

$$E_d = \frac{\mu_0}{4\pi} \sum_{i<j} \left(\frac{\vec{\mu}_i . \vec{\mu}_j}{r_{ij}^3} - 3 \frac{(\vec{\mu}_i . \vec{r_i})(\vec{\mu}_j . \vec{r_j})}{r_{ij}^5} \right) \tag{2.28}$$

where r_{ij} is the separation between the moments. The magnetic dipole interaction is a weak interaction compared to other interactions like the exchange interaction [28]. However, although the dipole interaction is a weak interaction, this interaction can play an important role in determining the magnetic ordering in crystals.

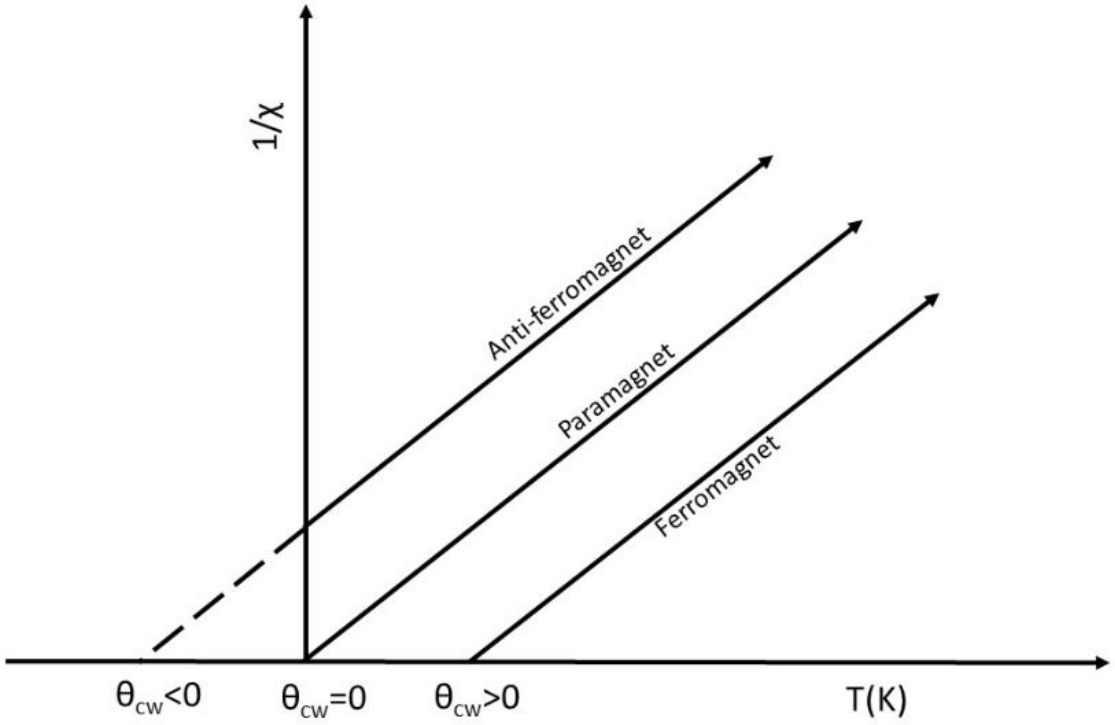

Figure 2.4: The high temperature inverse susceptibility for an antiferromagnet ($\theta_{CW} < 0$), a paramagnet ($\theta_{CW} = 0$), and a ferromagnet ($\theta_{CW} > 0$).

2.7 Heisenberg Model

We have discussed the various terms that enter into the description of a magnetic system. The exchange interaction has a quantum mechanical origin but it is often modelled using classical Heisenberg spins. A classical spin has unit magnitude and can lie anywhere on the surface of a sphere. Hence it can be described using the usual polar angle θ and azimuthal angle ϕ and has two degrees of freedom. A Hamiltonian which includes exchange, dipole interactions and an applied magnetic field can be written as

$$\mathcal{H} = -\sum_{i<j} J(r_{ij})\vec{S}_i.\vec{S}_j + \frac{\mu_0\mu_B^2}{4\pi}\sum_{i<j}(\frac{\vec{S}_i.\vec{S}_j}{r_{ij}^3} - 3\frac{(\vec{S}_i.\vec{r_i})(\vec{S}_j.\vec{r_j})}{r_{ij}^5}) - g_j\mu_B j\sum_i \vec{B}\cdot\vec{S}_i \quad (2.29)$$

where $\vec{S}_i$ are classical unit spins located at site i in a lattice.

2.8 Geometrical Frustration

In many materials, the exchange interactions between magnetic moments compete with one another such that a given moment cannot be either parallel or anti-parallel to its neighbours. This effect is called frustration and is often related to the geometry of the lattice on which the moments sit. Although the concept of frustration was first observed by Pauling in 1935 in water ice[29], it has been broadly studied in the context of spin glasses in 1970's [30].

In some materials, the geometrical structure is such that the classical spins are unable to simultaneously satisfy all antiferromagnetic interactions between them and at very low temperature these systems do not form long ranged ordered states [1]. However, for some other materials the system is able to minimise the energy but the ground state is not unique and can have a large ground state degeneracy.

In order to understand frustration, consider first an unfrustrated system such as a square lattice. This lattice has four spins located at the corners(Figure 2.5(a)). For

such a system it is possible to satisfy all antiferromagnetic interactions simultaneously with all spins anti-parallel, leading to a unique ground state. However, in case of a triangular structure, the three spins at the vertices of the triangle cannot all be anti-parallel. It is impossible to satisfy all antiferromagnetic interactions (Figure 2.5(b)) and the system is frustrated. However, the system can minimise it's energy by forming a 120^0 arrangement as shown in Fig. 2.6. This kind of unique ground state is not always possible for other frustrated magnetic systems such as the kagome and pyrochlore lattices. The geometrical structure is not the only cause of frustration. For example, in spin glasses the sites are randomly arranged and no regular ordered pattern is found resulting in a glass-like order.

In general, magnetic systems comprised of triangles and tetrahedra are frustrated. The ordering temperatures are often reduced compared to unfrustrated systems and the ground states can be highly degenerate[31]. Many of these magnetic systems exhibit unusual spin arrangements due to the contribution of the magnetic dipolar interaction. Quantum fluctuations and single ion anisotropy also play an important roles for these complex magnetic orderings at low temperature. Because of these interesting magnetic properties at low temperature, the search for new frustrated system is still on going. Recently, the family of rare earth compounds $SrLn_2O_4$ has been identified as a frustrated system. Extensive studies of $SrEr_2O_4$, $SrDy_2O_4$, $SrYb_2O_4$, $SrHo_2O4$ and $SrGd_2O_4$ have been carried out[32]. These systems will be discussed in the next chapter.

An empirical measure of frustration was introduced by Ramirez[33] to determine if a magnetic system is strongly frustrated or not. A frustration parameter is defined by the following formula[34]

$$f = -\frac{\theta_{CW}}{T_N} \tag{2.30}$$

where T_N is the transition temperature and θ_{CW} is the Curie-Weiss temperature.

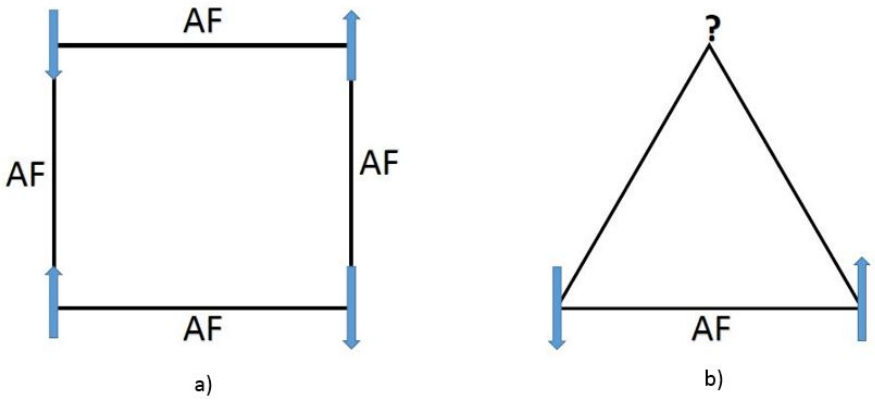

Figure 2.5: a) A simple unfrustrated 2d square lattice with antiferromagnetic interactions. The four spins at the corners are coupled antiferromagnetically and form an unfrustrated ground state. b) A triangular spin system with frustration. Spins at two vertices are arranged in an antiferromagnetic order but the third one is unable to satisfy antiferromagnetic coupling with the other two.

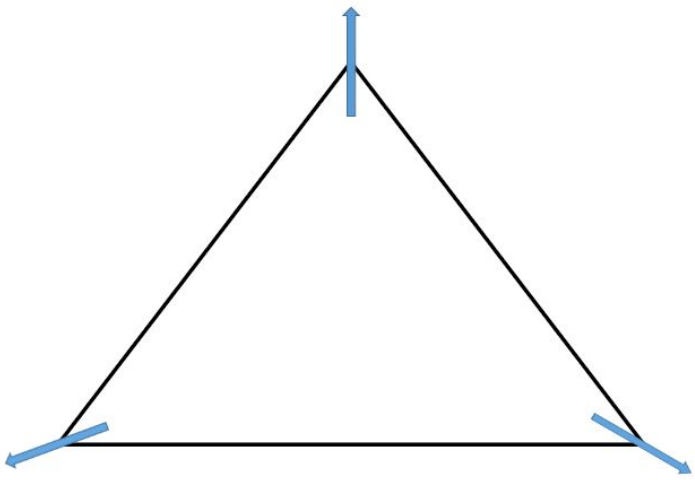

Figure 2.6: A triangular spin system can reach a ground state with spins in a plane oriented 120^0 apart from each other.

Table 2.1: Frustration Parameters

Materials	θ_{CW}	T_c	f	Ordering
VCl_2	-437	36	12	AF
$NaTiO_2$	-1000	< 2	> 500	-
$SrCr_8Ga_4O_{19}$	-515	3.5	150	SG
$MnIn_2Te_4$	-100	4	25	SG
Sr_2NbFeO_6	-840	28	30	SG

A value of $f > 1$ corresponds to a frustrated system. Generally, the system with $f > 5-10$ indicates strong frustration e.g strong denial of ordering. A list of strongly frustrated materials with frustration parameters are given in table 2.1.

For $SrGd_2O_4$, θ_{CW} and T_N are found to be $-10.3K$[1] and $2.73K$. Therefore the frustration parameter for $SrGd_2O_4$ is 3.77 and hence we expect significant frustration effects.

Chapter 3

RARE EARTH FAMILY OF COMPOUNDS

Compounds with the formula $SrLn_2O_4$(Ln=Lanthanide) consist of a network of linked hexagons and triangles which leads to unusual magnetic properties at low temperatures. The magnetic properties of each member of the family is different. Karunadasha et al. [32] characterized powder samples of $SrGd_2O_4$, $SrHo_2O_4$, $SrDy_2O_4$, $SrEr_2O_4$, $SrTm_2O_4$ and $SrYb_2O_4$ using magnetic susceptibility, magnetisation, and neutron diffraction. Their experiments identified the atomic structure and magnetic properties which indicated that strong geometric frustration effects were present in all members. Single crystals of the compounds $SrEr_2O_4$, $SrHo_2O_4$ and $SrDy_2O_4$ were also investigated at low temperatures by Petrenko [35, 36, 37, 38, 39] and more recently Young[1] has performed detailed studies on powder and single crystal samples of $SrHo_2O_4$ and $SrGd_2O_4$. Recent studies [40, 41, 42] of $SrDy_2O_4$ indicate field induced phase transitions at low T. In this chapter we summarize the atomic structure and the magnetic properties of the $SrLn_2O_4$ family of compounds.

3.1 Atomic Structure of $SrLn_2O_4$

The compounds $SrLn_2O_4$ crystallize in the form of calcium ferrite with space group Pnam[43]. Fig. 3.1 shows the structure of the $SrGd_2O_4$ compound which is representative of the entire family of compounds. In the ab plane, Gd^{3+} ions are linked in a network of hexagons and also linked by triangles along c axis. Two crystallographically inequivalent Gd^{3+} ions (blue and red in color) form two different triangular ladders along the c direction. These triangular "zigzag" chains are frustrated when

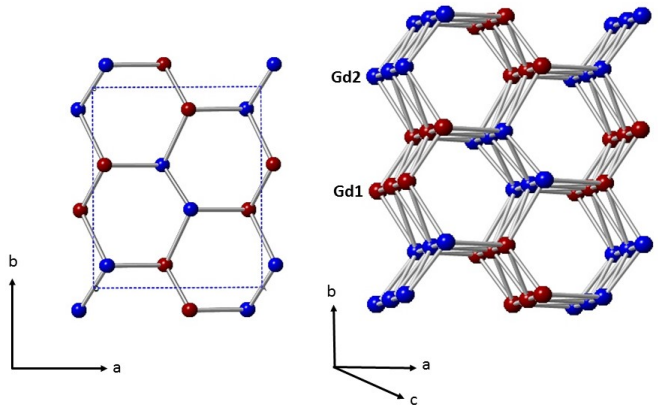

Figure 3.1: The left panel represents the two dimensional honeycomb structure of $SrLn_2O_4$. Red and blue colors represent the two inequivalent rare earth Ln^{3+} ions. The box indicates the unit cell. The right panel represents the three dimensional honeycomb structure of rare earth ions with chains of the two inequivalent Ln^{3+} ions running along the c axis.

antiferromagnetic interactions are considered between the spins. The "zigzag" chains can be viewed as linear chains with both first and second neighbour interactions [44].

3.2 Magnetic Properties of $SrLn_2O_4$

The magnetic order and susceptibility of the $SrLn_2O_4$ family of compounds with $Ln = Gd, Dy, Ho, Er, Tm$, and Yb were first investigated by Karunadasa et al.[32]. Table 3.1 gives the effective moments and Curie-Weiss temperatures determined from the high T susceptibility measurements. In all cases θ_{CW} is negative indicating that antiferromagnetic interactions are dominant. The magnetisation versus applied field measurements indicated various complex transitions at low temperatures. Figure 3.2 shows the magnetisation as a function of applied field at $1.8K$ for powder samples. In the cases of $Ln = Yb, Gd$ and Tm the magnetisation per Ln atom increases slowly as

Table 3.1: Moments and Curie-Weiss Temperatures of $SrLn_2O_4$ Compounds

Compound	$\mu_{eff}(\mu_B)$	θ_{CW}
$SrGd_2O_4$	8.02(2)	-9.0(6)
$SrDy_2O_4$	10.35(1)	-22.9(5)
$SrHo_2O_4$	10.50(1)	-16.9(5)
$SrEr_2O_4$	9.176(3)	-13.5(2)
$SrTm_2O_4$	7.51(1)	-33.8(6)
$SrYb_2O_4$	4.348(6)	-99.4(7)

a function of applied field, reaching 1 to 2.5μ_B at a field of 7 T. For Dy, Er and Ho, the magnetisation reached about 5 to 6μ_B at the same field. These results indicate that the systems are far from saturation at this field value. The derivative of the magnetisation with respect to field $\frac{dM}{dH}$ is shown in Fig. 3.3 corresponding to the curves in Fig. 3.2. Gd, Tm, and Yb show monotonic behaviour but Ho, Dy, and Er exhibit peaks which suggest some kind of metamagnetic behaviour at low fields.

Most of the $SrLn_2O_4$ compounds do not exhibit magnetic long range order at temperatures expected from their Curie-Weiss temperatures. A recent study of $SrHo_2O_4$ and $SrGd_2O_4$ in their single crystal and polycrystalline forms was carried out by Olga Young[1] for her PhD research. Her studies indicated that $SrHo_2O_4$ has a low dimensional character with no long range order [45]. This was attributed to strong antiferromagnetic interactions within the "zig-zag" chains but extremely weak interactions between the chains. $SrHo_2O_4$ also exhibits strong anisotropy behaviour in an applied field which is likely due to crystal field effects. This behaviour was also previously observed in $SrEr_2O_4$[36, 46, 31, 38]. Fig. 3.4 shows the structures of $SrHo_2O_4$ and $SrEr_2O_4$ where only one of the lanthanide "zigzag" chains is ordered with ferromagnetic chains arranged antiferromagnetically along the c axis.

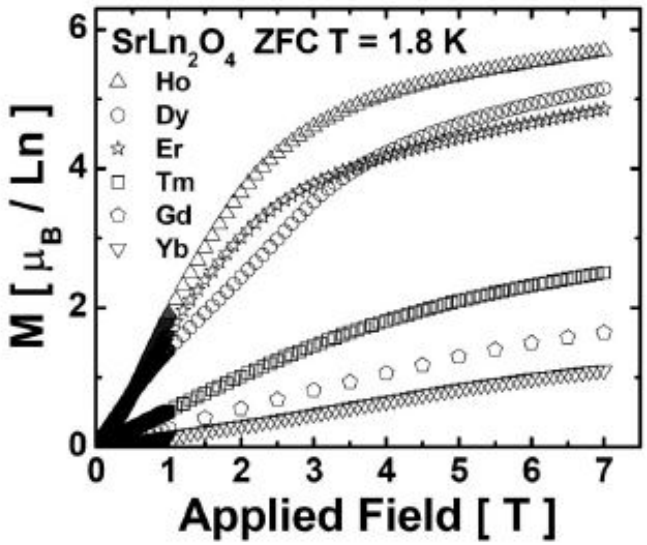

Figure 3.2: Field dependent magnetisation plots of $SrLn_2O_4$. At temperature T=1.8K magnetisation increases slowly with field for Gd, Yb and Tm whereas for Ho, Dy and Er magnetisation increases repidly up to $H = 2.5T$ and then saturates at $H = 7.0T$. Reprinted with permission from the American Physical Society.

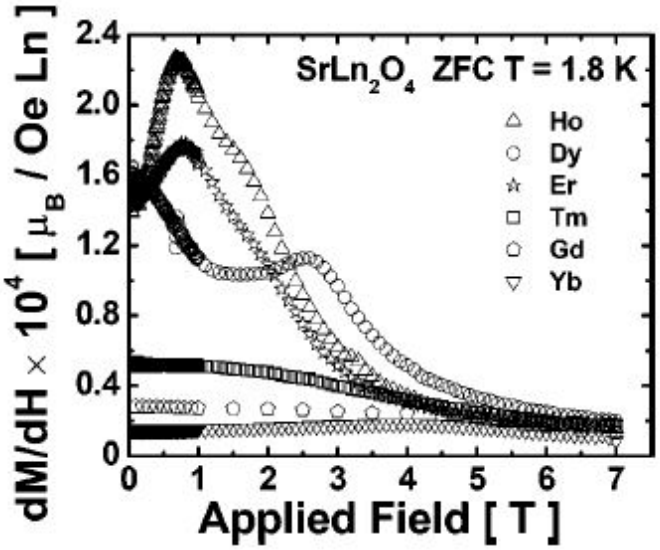

Figure 3.3: Field dependent magnetisation derivatives with respect to applied field of $SrLn_2O_4$. Reprinted with permission from the American Physical Society.

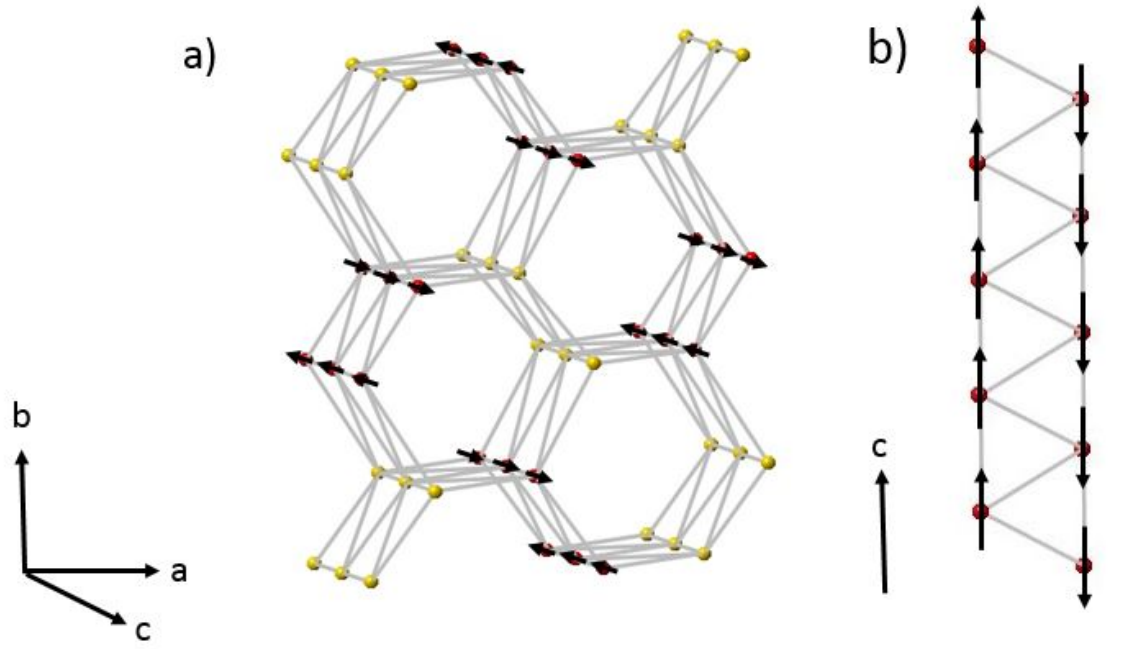

Figure 3.4: Left panel represents the magnetic structure of $SrEr_2O_4$ determined from neutron diffraction patterns at $T = 0.55K$ and the right panel represents the triangular ladder run along c axis.

In contrast, the $SrGd_2O_4$ compound exhibits two phase transitions at finite temperatures even though it has the smallest Curie-Weiss temperature in the family. The low temperature properties of $SrGd_2O_4$ differ from any other compounds of the $SrLn_2O_4$ family. Specific heat, magnetisation and susceptibility measurements on both powder and single crystal samples indicate several low temperature transitions. Measurements of the magnetisation as a function of an applied magnetic field along the c axis were employed to map out a phase diagram in the $H - T$ plane. However, the details of these phases remain unknown. Each member of the $SrLn_2O_4$ family of compounds exhibits different magnetic behaviour even though the crystal structure is the same. $SrGd_2O_4$ is special since, in the ground state, the Gd^{3+} ion has $L = 0$ and thus crystal field effects are not expected to be important. This material should

provide an example of a system with classical Heisenberg magnetic moments.

3.3 Crystal Structure of $SrGd_2O_4$

The atomic positions of the $SrGd_2O_4$ compound are identified at sites $4c(x, y, 0.25)$ in the unit cell of the Pnam space group and are given in Table 3.2. The orthorhombic unit cell has lattice parameters a, b and c with values $10.1321(1)A^0$, $12.0614(1)A^0$ and $3.47566(2)A^0$ respectively[1]. The unit cell contains four Sr atoms, eight Gd atoms (four on each inequivalent site), and sixteen oxygen atoms on 4 inequivalent sites. Figure 3.5 shows the arrangement of atoms in the unit cell. The Sr atoms sit at the center of the honeycomb structure formed by $Gd1$ and $Gd2$.

Both direct exchange and superexchange contribute to the interactions between the magnetic sites. Superexchange is possible along the b direction since $Gd1 - Gd1$ and $Gd1 - Gd2$ share bonds with the $O2$ and the $O3$ sites respectively. $Gd2 - Gd2$ sites in this direction share bonds with the $O4$ sites. Along the a direction, $O1$ sites are shared by $Gd1 - Gd2$ sites. Along the c direction, the $Gd1 - Gd1$ sites share bonds with the $O2$ and $O3$ sites whereas the $Gd2 - Gd2$ sites share bonds with the $O1$ and $O3$ sites. Each magnetic site has eight nearest neigbours.

3.4 Magnetic Properties of $SrGd_2O_4$

Bulk property measurements of thermodynamic quantities such as the specific heat, susceptibility, magnetisation and its derivative with respect to applied field obtained by Young et. al.[16] for single crystal samples are shown in figures 3.6 to 3.12 in the following subsections.

3.4.1 Temperature and Field Dependence of Susceptibilities

Temperature dependent susceptibilities of a single crystal sample of $SrGd_2O_4$ are shown in Fig. 3.6 for applied fields along the three principal axes. The top panel shows

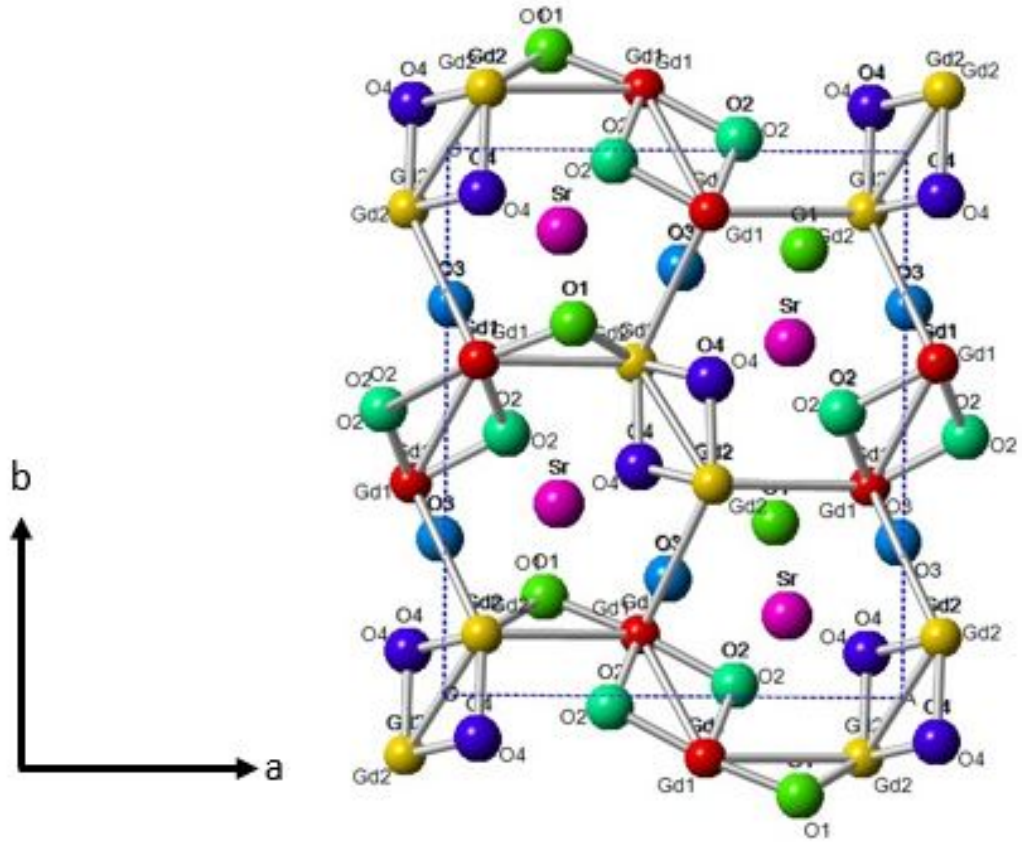

Figure 3.5: Three dimensional structure of $SrGd_2O_4$. Four types of O atoms sit in different positions connecting the Gd^{3+} atoms making different angles and provide superexchange pathways in addition to direct exchange. Red and orange colors represent Gd1 and Gd2. The O1,O2,O3 and O4 represent green, light green, light blue and blue colors respectively. Central Sr atom is represented by pink color

Table 3.2: Crystal Structure Parameters for $SrGd_2O_4$

Element	x	y
Sr	0.7506(5)	0.6489(4)
Gd1	0.4270(4)	0.1127(3)
Gd2	0.4161(4)	0.6110(3)
O1	0.220(3)	0.181(2)
O2	0.135(3)	0.479(3)
O3	0.510(3)	0.785(2)
O4	0.423(4)	0.420(2)

χ in a field of $1kOe = 0.1T$ and the bottom panel shows the inverse susceptibility χ^{-1}. According to Hund's rules, the Gd^{3+} free ions have $l = 0$, $s = 7/2$, $j = 7/2$ and hence $g_j = 2$. The predicted effective moment $\mu_{eff} = g_j\mu_B\sqrt{j(j+1)}$ is $7.94\mu_B$. A linear fit to χ^{-1} yielded $\mu_{eff} = 8.03(1)\mu_B$ and $\theta_{CW} = -10.3(2)K$. These results indicate that crystal field effects should be minimal and that antiferromagnetic exchange is dominant.

Fig. 3.7 shows the low temperature susceptibility for a single crystal in a $100Oe(0.01T)$ field. There appears to be a small cusp in χ for the a and b directions at $T = 2.73K$ and a large decrease in χ for a field along the c axis at this temperature. This behaviour is indicative of a phase transition to long range antiferromagnetic order. There is an upturn in χ at the lowest measured temperature $T = 0.48K$ which may indicate a second transition at lower values of T.

Figure 3.8 shows the low temperature susceptibility for increasing applied fields. For applied fields along the a and b directions (top panel), there is little change except at the very lowest temperature. However, in case of fields along the c direction the transition at $T = 2.73K$ moves to lower T and the transition is gradually suppressed.

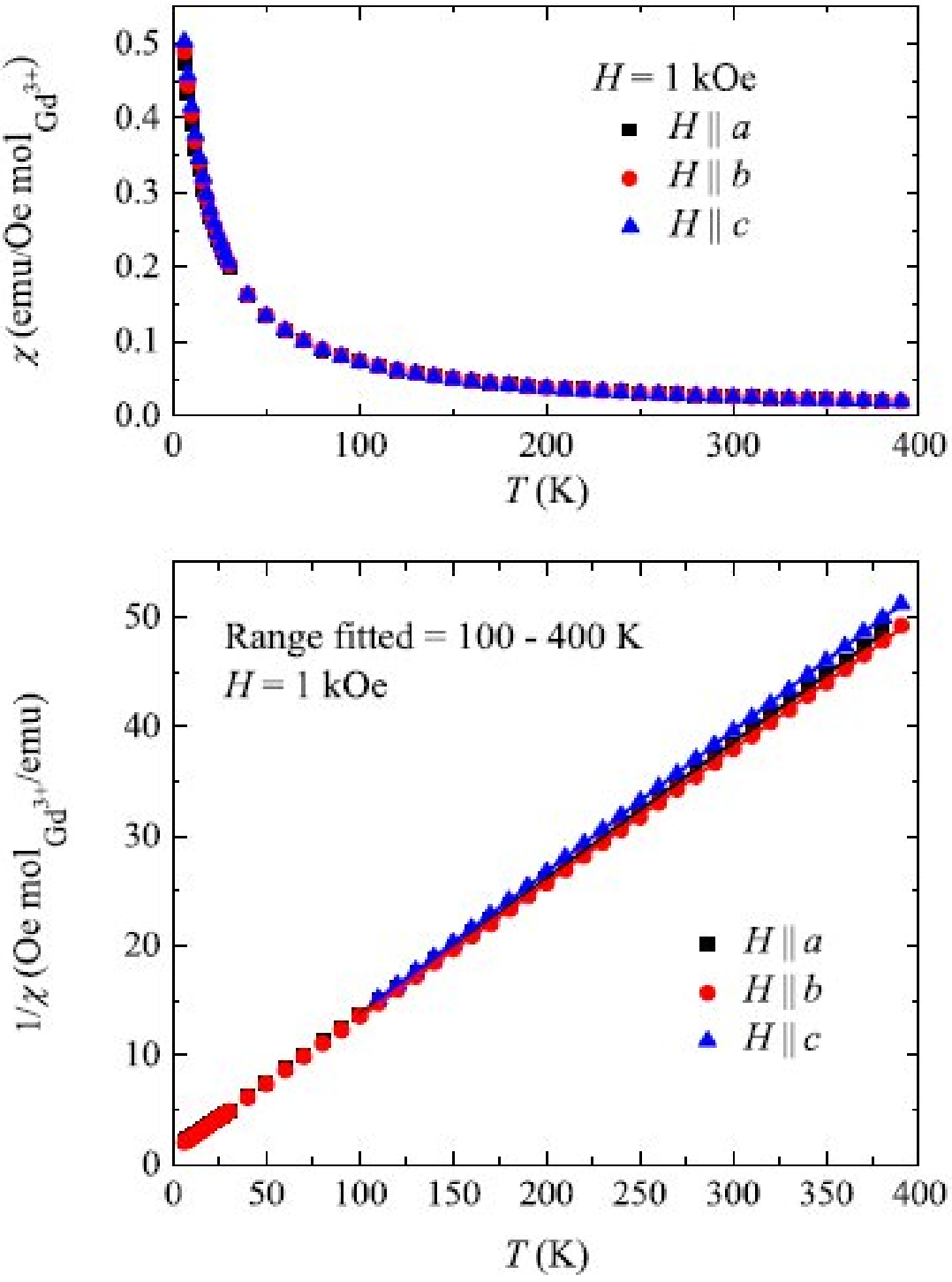

Figure 3.6: High temperature susceptibility of $SrGd_2O_4$ for a field $1kOe(0.1T)$ applied along the three principal axes. The upper panel shows $\chi(T)$ and the lower panel shows $\chi^{-1}(T)$. Reprinted with permission from the American Physical Society.

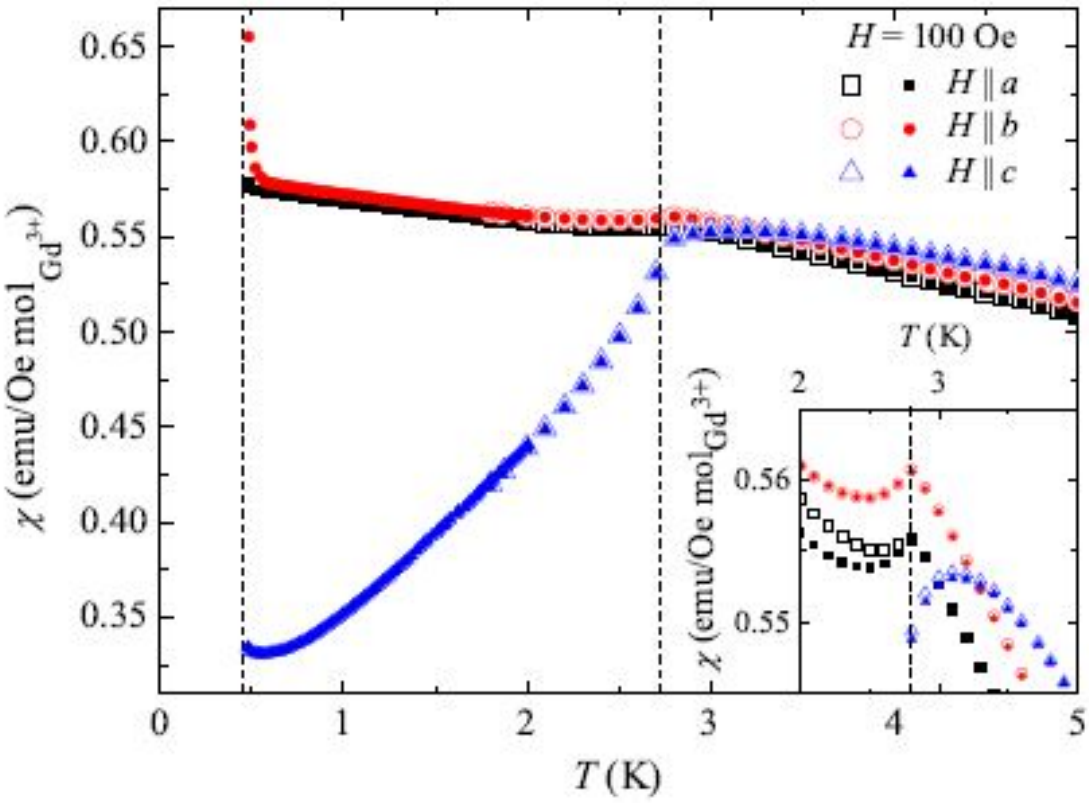

Figure 3.7: Low temperature susceptibility $\chi(T)$ in a field of $100Oe(.01T)$ along the three principal axes. Reprinted with permission from the American Physical Society.

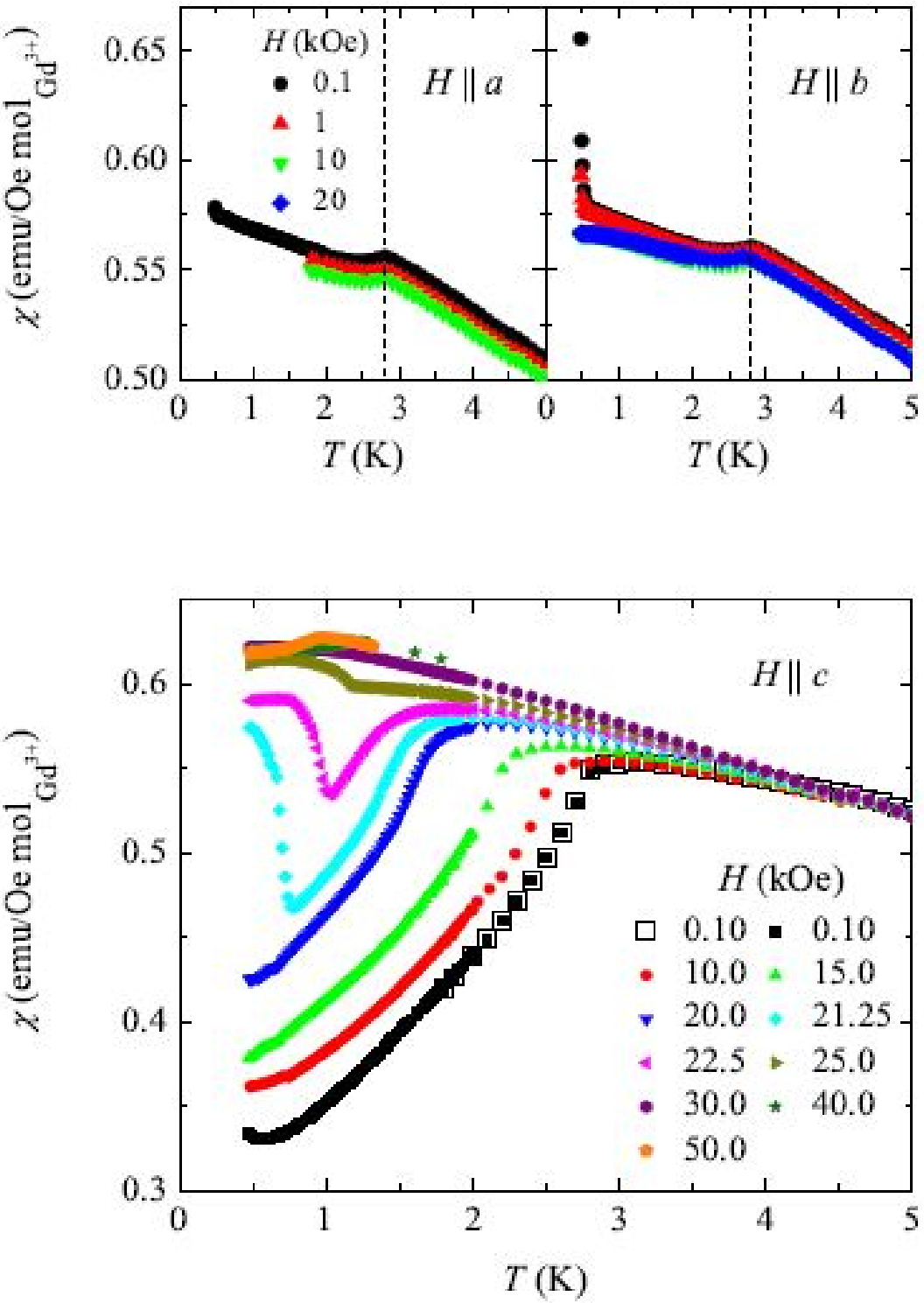

Figure 3.8: Temperature dependent susceptibility for different fields along a and b axes(top panel). Bottom panel represents χ vs T plot for different fields along the c direction. χ shows similar behavior for both a and b directions but behaves differently in the c direction. Reprinted with permission from the American Physical Society.

3.4.2 Field Dependence of Magnetisation

Figure 3.9 shows the magnetisation(top panel) and its derivatives (bottom panel) as a function of the applied field along the three principal axes at $T = 0.5K$. The magnetisation measurement does not show any significant feature for fields along the a and b directions, even up to a field of 70 kOe =7 T. In fact, at these higher fields, the magnetisation reaches saturation for both $H \parallel a$ and $H \parallel b$. However, for an applied field along c direction, the magnetisation derivative shows a sharp peak at $H_{c1} = 20kOe$. Additional small peaks at $H_{c2} = 23.3kOe$ and $H_{c3} = 53.3kOe$ are also present. The average magnetisation between H_{c1} and H_{c2} is $2.3\mu_B$ which is close to 1/3 of the saturation value $g_j\mu_B J = 7\mu_B$. This value is suggestive of a *two-spins-up-one-spin down* (uud) structure on the triangular chains. At the field H_{c3}, the magnetisation is close to saturation.

3.4.3 Temperature Dependence of Specific heat

Fig. 3.10 shows the specific heat C/T measured in zero applied field as a function of temperature. Two transitions to long range order are observed at $T = 2.73K$ and $T = 0.48K$. The magnetic component was obtained by subtracting the lattice contributions of two nonmagnetic isostructural compounds SrY_2O_4 and $SrLu_2O_4$. By integrating C/T the magnetic entropy $S = R\ln(2J + 1) = R\ln 8$ is approached at $6K$. The specific heat was also measured both as a function of applied field along the c direction and temperature for a range of field strengths and temperatures. In the top panel of Fig. 3.11, the two transitions observed in zero field as a function of T move closer together and merge into a single peak at about $22.5kOe$. In the bottom panel, plots of C/T as a function of $H \parallel c$ exhibit two peaks at low T which merge together as the temperature approaches $T \sim 1.4K$

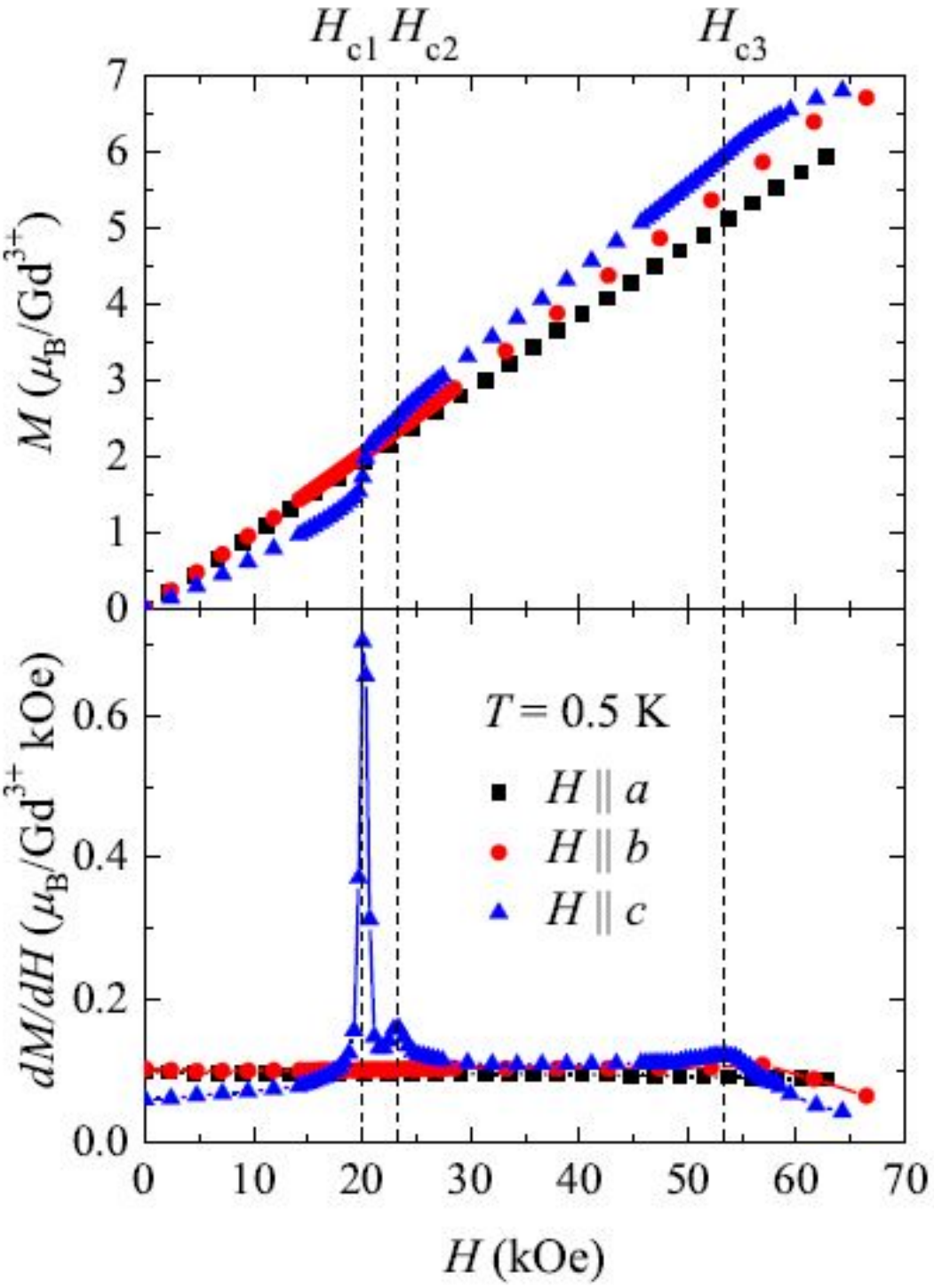

Figure 3.9: Field dependent magnetisation and its derivative for fixed temperature. For temperature $T = 0.5K$ two peaks in the magnetisation derivative for $H \parallel c$ are observed. Reprinted with permission from the American Physical Society.

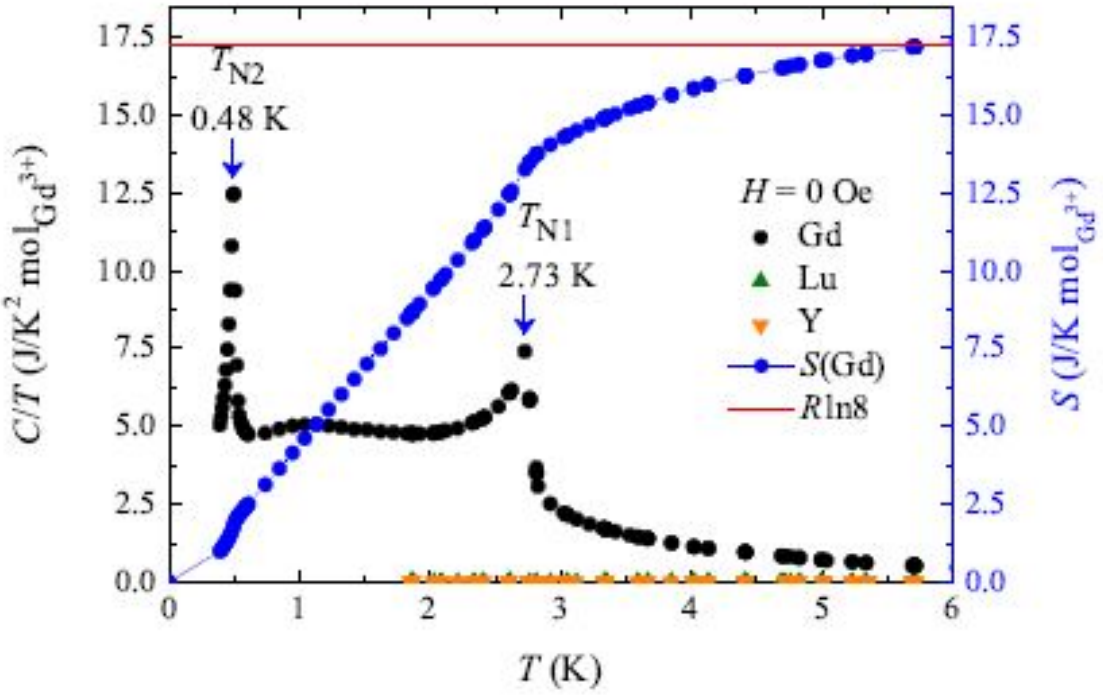

Figure 3.10: Specific heat as a function of temperature in zero applied field. Two transitions are observed at $0.48K$ and $2.73K$. The entropy S is also plotted as a function of T and saturates near $T = 6K$. Reprinted with permission from the American Physical Society.

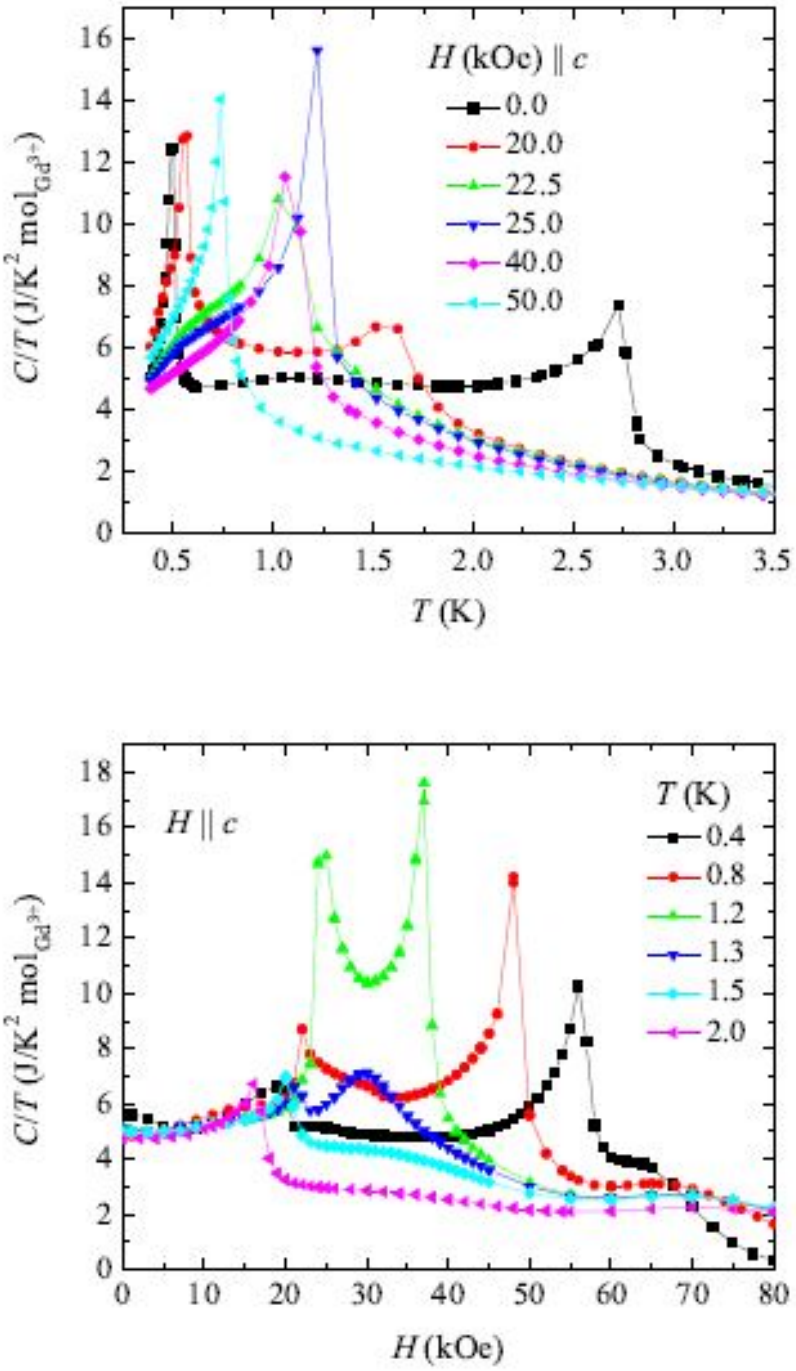

Figure 3.11: Top panel represents temperature dependent C/T for several applied fields. At zero field two peaks in C/T are well separated for $H \parallel c$. Bottom panel represents C/T as a function of field along c direction for different temperatures. Reprinted with permission from the American Physical Society.

3.4.4 H-T Phase Diagram of $SrGd_2O_4$

A $H-T$ phase diagram was constructed from susceptibility, magnetisation and specific heat data as shown in Fig. 3.12 for $H \parallel c$. Using these bulk property measurements of $SrGd_2O4$, four separate phases were identified in addition to the paramagnetic phase. At low temperature, two ordered phases are evident and, at temperatures above $T = 1.33K$, there is only one ordered phase. The inset shows the results for $H \parallel a, b$ where there appears to be only one ordered phase. The detailed nature of these ordered phases is presently unknown. Neutron diffraction measurements have not been carried out as yet but they could shed light on the nature of the order.

In the next chapter we introduce a model Hamiltonian to describe the magnetic properties of $SrGd_2O_4$. We will study the model using Monte Carlo methods and compare the results to the experimental measurements described above.

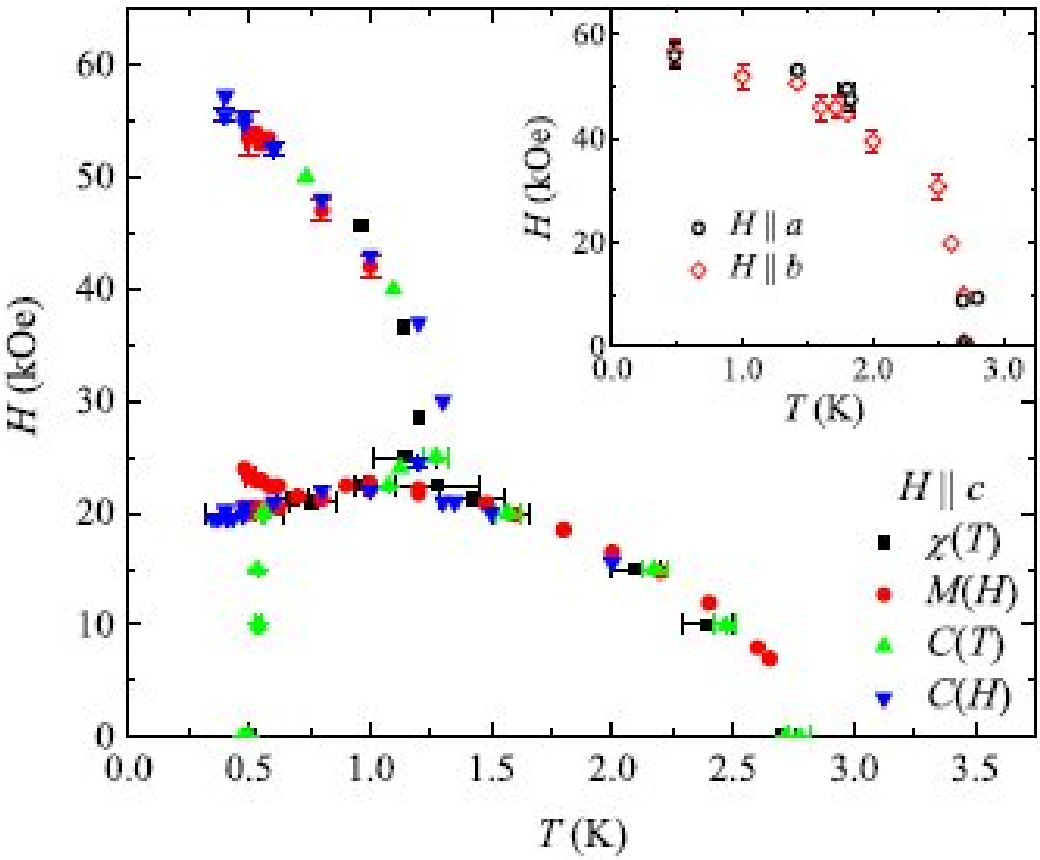

Figure 3.12: $H - T$ phase diagram of $SrGd_2O_4$ from magnetisation, susceptibility and specific heat data for field $H \parallel c$. Reprinted with permission from the American Physical Society.

Chapter 4

MODEL HAMILTONIAN AND MONTE CARLO METHODS

4.1 Model Hamiltonian

In this section we discuss a model Hamiltonian to describe the magnetic properties of $SrGd_2O_4$. We will include exchange interactions, the Zeeman interaction with external fields as well as the magnetic dipole-dipole interaction. Since crystal field effects for Gd are not important, the next most important term is the dipolar term. The rather large magnetic moment of Gd and the rather small lattice spacing in the c direction means that this term should be included. We will use classical 3-component unit vectors $\vec{S}_i$ to model the spins on the Gd sites. The Hamiltonian has the form

$$\mathcal{H} = -\sum_{i<j} J_{ij}\vec{S}_i.\vec{S}_j + g_d \sum_{i<j}\left[\frac{\vec{S}_i.\vec{S}_j}{r_{ij}^3} - \frac{3(\vec{S}_i.\vec{r}_{ij})(\vec{S}_j.\vec{r}_{ij})}{r_{ij}^5}\right] - \vec{H}.\sum_i \vec{S}_i \tag{4.1}$$

where the first term is the exchange energy term. The exchange parameters J_{ij} represent the interaction strength between the neighbouring spins at sites i and j. The values of the J_{ij} vary depending on the distances between the spins. The negative sign is convention and positive values of J_{ij} indicate that the interaction is ferromagnetic whereas the negative values of the J_{ij} indicate that the interaction is antiferromagnetic. The second and third terms are the dipolar and Zeeman contributions to the Hamiltonian respectively. The strength of the dipolar interaction is indicated by g_d and $\vec{r}_{ij}$ is the distance between the spins measured in units of $c = 3.476A^0$. The units of J_{ij}, H and g_d are in ${}^0K$. The value of $g_d = \frac{\mu_0\mu_{eff}^2}{4\pi c^3 k_B} = 0.95K$. The parameter H in

the Zeeman term can be converted to Tesla by dividing by $\mu_{eff}/k_B = 5.37$

As was shown previously in Fig. 3.1, the Gd sites lie on triangular "zigzag" chains along the c direction which are linked by hexagons in the ab plane. Fig 4.1 shows the unit cell with the eight Gd atoms. We label these as sublattices $i = 1..8$. The hexagons are not planar but rather undulate up and down along the c axis by $\pm c/4$ and the nearest neigbour distances are not all equal. The $\pm$ signs on the sublattice indices indicate which sites are displaced up and down. Each of the magnetic sites in $SrGd_2O_4$ has eight nearest neighbours. Both the Gd_1 and Gd_2 sites have four neighbours on $Gd1$ sites and four on $Gd2$ sites. For example the $Gd2$ site labelled as $6-$ has two $Gd2$ neigbours on the same sublattice above and below at distance $\pm c$ along the c axis. There are also two $Gd2$ neighbours on sublattice 4 at $\pm c/2$ which connect the rungs on the $Gd2$ triangular chain. The remaining four $Gd1$ neigbours are on sublattices 5 and 8 at $\pm c/2$ and are the rungs connecting the $Gd2$ and $Gd1$ chains. The shortest distance(3.476 A^0) is measured along c direction for $Gd1 - Gd1$ or $Gd2 - Gd2$ and the largest distance(4.081 Å) for $Gd1 - Gd2$ is in the vertical direction in Fig. 4.1. In the horizontal direction the $Gd1 - Gd2$ distance is 3.887 A^0. The $Gd1 - Gd1$ and $Gd2 - Gd2$ distances in the vertical direction are 3.550 A^0 and 3.617 A^0 respectively. Hence we have six different exchange parameters coupling the nearest neighbours.

Table 4.1 gives the values of the exchange parameters that we have used in our simulations. Since the interactions involve both direct and superexchange, we have no direct information about their values. We have simply chosen values that give qualitative agreement with the experimental results.

The dipolar interaction is long ranged but we will only consider the interaction between the eight nearest neighbour sites. The contribution from further neighbours is very small and our calculations have indicated that they do not impact our results.

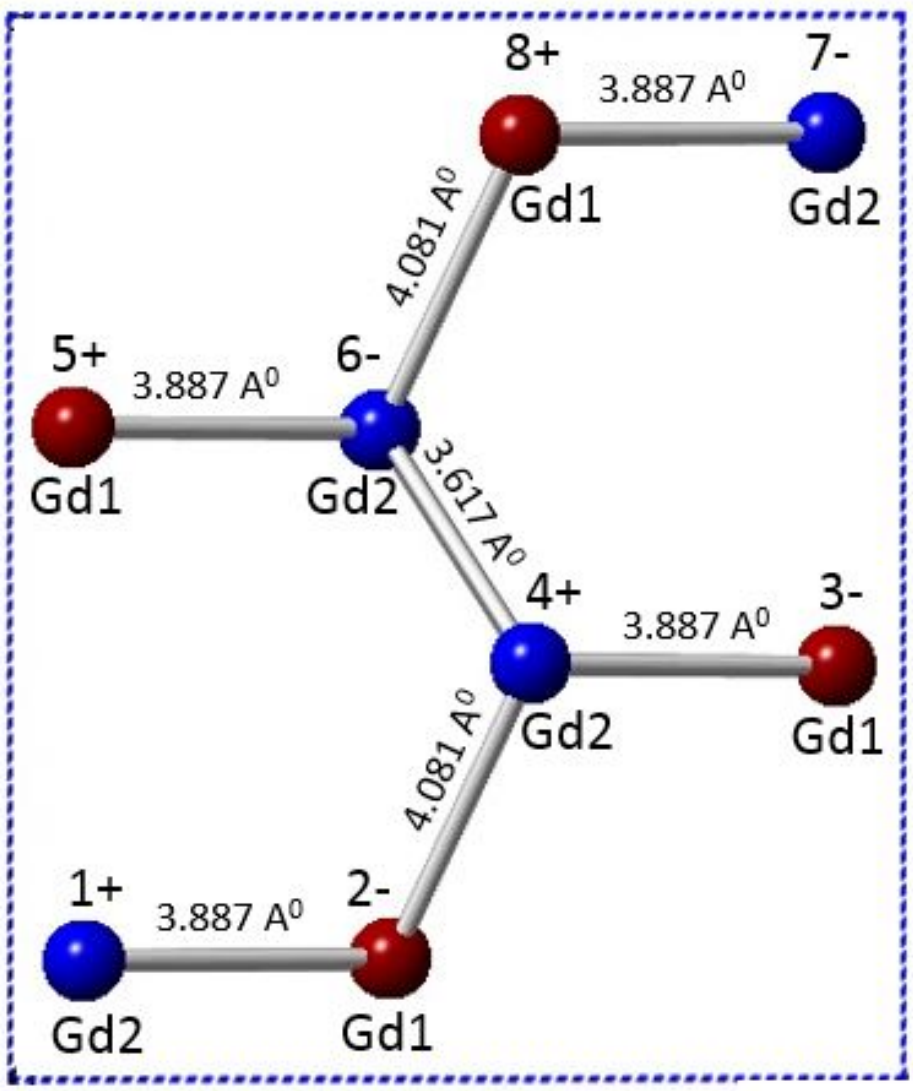

Figure 4.1: The unit cell of $SrGd_2O_4$ indicating the two inequivalent Gd sites as $Gd1$ (red) and $Gd2$ (blue). The sites have sublattice labels $i = 1..8$ and the $\pm$ signs indicate the direction of displacement of the sites along the c axis.

Table 4.1: Exchange Parameters for $SrGd_2O_4$

Interaction	Distance(A^0))	$J_{ij}(^0K)$
$Gd1 - Gd1$	3.476	-1.25
$Gd2 - Gd2$	3.476	-4.25
$Gd1 - Gd1$	3.550	-3.75
$Gd2 - Gd2$	3.617	-2.75
$Gd1 - Gd2$	3.887	+1.25
$Gd1 - Gd2$	4.081	-2.25

4.2 Basic Statistical Mechanics

The primary concern of the statistical mechanics is the calculation of the properties of many body systems consisting of $10^{23} \sim 10^{24}$ particles[47]. The goal is to calculate the macroscopic properties such as internal energy E, entropy S and the specific heat C_v of a system. The system is described by a Hamiltonian which can be used to find the total energy of any particular state of the system. In thermal equilibrium at temperature T, the probability for the system to exist in a particular state s is described by the Boltzmann distribution

$$P_s = \frac{1}{Z} e^{-\frac{E_s}{k_B T}} \tag{4.2}$$

where

$$Z = \sum_s e^{-\frac{E_s}{k_B T}} \tag{4.3}$$

is the canonical partition function, k_B is the Boltzmann constant whose value is 1.38 $\times$ 10^{-23} J $K^{-1}$and E_s is the energy of the state s.

The expectation value of a thermodynamic quantity Q for an equilibrium system can be calculated as

$$< Q >= \sum_s Q_s P_s = \frac{1}{Z} \sum_s Q_s e^{-\beta E_s} \tag{4.4}$$

where Q_s is its value in state s and $\beta = \frac{1}{k_B T}$.

The Helmholtz free energy F is

$$F = E - TS \tag{4.5}$$

where E and S are the internal energy and entropy respectively. In terms of partition function Z, the free energy can be expressed as

$$F = -k_B T ln Z \tag{4.6}$$

and the internal energy and specific heat are obtained as follows

$$E = -\frac{\partial}{\partial \beta}(ln Z) \tag{4.7}$$

$$C_v = -k_B \beta^2 \frac{\partial E}{\partial \beta} = k_B \beta^2 \frac{\partial^2}{\partial \beta^2}(ln Z) \tag{4.8}$$

With an applied field H, the magnetisation M is given by

$$M = \frac{1}{\beta} \frac{\partial}{\partial H}(ln Z) \tag{4.9}$$

and the derivative of magnetisation with respect to field yields the magnetic susceptibility χ

$$\chi = \frac{\partial M}{\partial H} = \frac{1}{\beta} \frac{\partial^2}{\partial H^2}(ln Z) \tag{4.10}$$

Hence all the thermodynamic properties can be obtained from the free energy F or the partition function Z by taking appropriate derivatives.

4.2.1 Phase Transitions

A phase transition occurs when a system abruptly changes from one type of order, or phase, to another. We are all familiar with phase transitions in a water system: the liquid phase turns into vapor when it is heated through the boiling temperature and turns into ice when it is cooled through the freezing temperature. Similar phase changes occur in magnetic systems and these transitions are accompanied by abrupt changes in their thermodynamic quantities. Changes in temperature T or applied fields H can produce a phase transition from one type of magnetic spin ordering to another type of ordering. Phase transitions can be classified as first order or second order. A first order transition occurs if the first derivative of the free energy F with respect to a thermodynamic parameter is discontinuous whereas the second derivative of free energy is singular for a second order phase transition.

A phase transition is often accompanied by a spontaneous symmetry breaking when changing from a disordered state to an ordered state. Order parameters characterize the ordered state and acquire nonzero values at the transition. Generally, phase transitions are found in different types of systems such as ferromagnets, antiferromagnets, liquid crystals and superconductors. The order parameter can be a scalar, vector or even a tensor. In our case the order parameter is related to the classical spins which can have any direction on the surface of a sphere. In the disorered high temperature phase, the directions of all the spins are random and there is no net magnetic moment $\vec{M} = \sum_i \vec{S}_i$. However, due to exchange interactions between the spins, they can abruptly align at a lower temperature to form a net moment such as in a fridge magnet. This alignment occurs at a critical temperature T_C below which the system has long range magnetic order.

This singular behavior is characterized by critical exponents. Near the phase transition, the thermodynamic quantities vary as a power of the deviation from the critical value of the thermodynamic parameter . For example, the specific heat,

susceptibility and magnetisation vary as a power of $t = \frac{T-T_C}{T_C}$

$$\begin{aligned} C_v &\sim |t|^{-\alpha} \\ \chi &\sim |t|^{-\gamma} \\ m &\sim |t|^{\beta} \end{aligned} \tag{4.11}$$

where α, γ, and β are critical exponents. The values of the critical exponents depend on both dimension D of the model and the symmetry of the order parameter but are independent of other details of the system. For example, the Ising model only has a discrete up-down symmetry which corresponds to a spin with only one component. The Heisenberg model has three component spins which lie anywhere on the surface of a sphere. The $D = 3$ Ising model has exponent values $\alpha = +.110, \beta = .325, \gamma = 1.24$ whereas the $D = 3$ Heisenberg model has exponents $\alpha = -.112, \beta = .361, \gamma = 1.39$[48]. Hence the two models differ in that the singular part of the specific heat is divergent in the Ising case and not in the Heisenberg case.

4.3 Monte Carlo Simulation

In general, the partition function cannot be calculated exactly except for a rather few low dimensional cases and numerical methods are needed. Monte Carlo simulation is based on using random numbers to explore the states of complex systems. In this method a sequence of configurations is generated to access all important states of the system and thermodynamic averages are calculated. A Markov chain process is followed to select the important states. We will describe two common methods used in Monte Carlo simulations: the Metropolis method[49] and the heat bath method[50].

4.3.1 Markov Chain

To perform a Monte Carlo simulation, it is essential to generate states using random numbers. A Markov process is used to generate a state U from a current state W

with transition probability $T(W \rightarrow U)$ which must obey the following conditions

1. Transition probability should be independent of the transition step.

2. The probability depends only on states U and W and not any other previous states or configurations.

By this process, a sequence of states is generated known as a Markov chain. Another important constraint that must be satisfied is the closure relation that the probability of transition from state W to state U obeys

$$\sum_{U} T(W \rightarrow U) = 1 \tag{4.12}$$

In Monte Carlo simulations, a Markov process is used to generate a chain of states. Starting from an initial random state W, following the above process a new state U is generated and then the next state V is generated from the state U and so on. If the process is repeated many times it eventually approaches an equilibrium distribution provided the transition probability is chosen properly. To achieve equibilium, two conditions are required: ergodicity and detailed balance.

4.3.2 Ergodicity

The ergodicity condition states that all states of a system must be accessible from any other state if the simulation is allowed to run for a sufficiently long time. That means there must be at least one path to reach every other possible state from each state. The ergodicity condition is essential because to get a correct equilibrium probability distribution, all generated states must have non zero probability. If any of the states is inaccessible, the transition probability from one state W to another state U in our Markov chain process could be zero. However, there must be at least one definite path that allows us to reach the new state with non zero probability.

4.3.3 Detailed Balance

Detailed balance is another condition that is incorporated into a Markov chain. Detailed balance ensures that an equilibrium distribution is approached after many Markov steps. If we regard the process as a time evolution for the probability $P_W(t)$ of state W at time t, then the master equation is

$$\frac{dP_W(t)}{dt} = -\sum_U T(W \to U)P_W(t) + \sum_U T(U \to W)P_U(t) \tag{4.13}$$

In equilibrium the two terms on the right side cancel and we obtain an equilibrium probability distribution for the states $\tilde{P}_W$. This condition is satisfied if we have

$$\tilde{P}_W T(W \to U) = \tilde{P}_U T(U \to W) \tag{4.14}$$

and is called detailed balance. It simply states that in equilibrium the are as many transitions into a given state as out of it.

If we rearrange eqn 4.14, then the ratio of the transition probabilities for any two states is related to the ratio of their equilbrium probabilities which for the Boltzmann distribution becomes

$$\frac{T(W \to U)}{T(U \to W)} = \frac{\tilde{P}_U}{\tilde{P}_W} = exp\left[\beta(E_W - E_U)\right] \tag{4.15}$$

4.4 Monte Carlo Algorithms

In magnetism studies, the most commonly used Monte Carlo algorithms are the Metropolis and heat bath methods.

4.4.1 Metropolis Algorithm

The Metropolis algorithm was first introduced by Metropolis in 1953[49]. In this method, for each transition from one state to the next, the transition probability is

chosen to be

$$\begin{aligned} T(U \to W) &= \frac{1}{\tau_0} e^{-(\beta \Delta E)} \quad \Delta E > 0 \\ &= \frac{1}{\tau_0} \qquad\qquad \Delta E < 0 \end{aligned} \tag{4.16}$$

where τ_0 is the time for the transition to occur.

The following steps are performed in a single spin flip Monte Carlo algorithm.

1. Select an initial micro state U and calculate energy E_U for this state.

2. Choose a random spin and change it's direction forming a new state W.

3. Calculate the energy for new state E_W.

4. If $E_W > E_U$, accept the new state if the acceptance ratio $e^{-\beta \Delta E}$ is greater than a random number between 0 and 1, otherwise reject it and remain in the same state.

5. Go back to step 2.

This process is carried out over the entire lattice which is called a Monte Carlo step. In the Metropolis algorithm, the new directions of the spins are updated randomly within a range of acceptance that leads to the rejection of states. In our work we will use the heat bath method. Although it requires more computation compared to Metropolis method, no moves are rejected.

4.4.2 Heat Bath Method

The heat bath method is easily implemented for a classical Heisenberg spin system[50]. The heat bath method is used to generate a sequence of spin states to sample the thermodynamics of the system in thermal equilibrium.

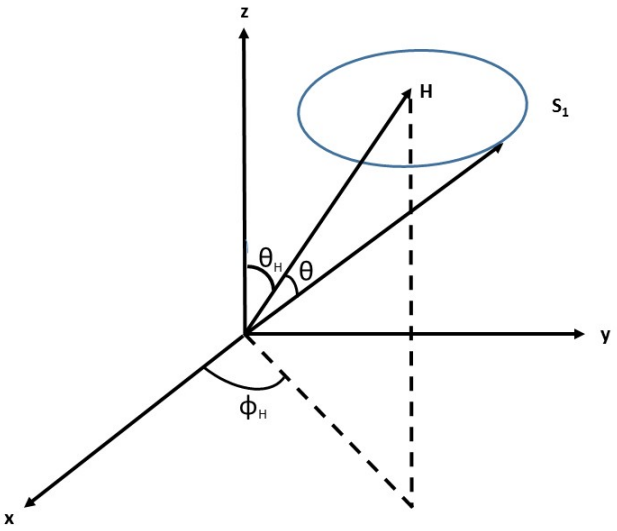

Figure 4.2: A single classical spin $\vec{S}$ of unit length in magnetic field $\vec{H}$. The direction of the field with respect to global coordinates is described by θ_H and ϕ_H. The direction of the spin with respect to the direction of $\vec{H}$ is denoted by θ.

Consider first a single classical spin of unit length in the presence of a field $\vec{H}$ as shown in figure 4.2. The energy is $-\vec{H}.\vec{S} = -H\cos\theta$ where θ is the angle between the directions of the spin and the field. We can choose to describe the direction of the spin with respect to the field direction using the angles θ and ϕ. The normalized Boltzmann probability for the spin direction is

$$P(\theta,\phi) = \frac{\beta H e^{\beta H\cos\theta}}{4\pi\sinh(\beta H)} = P_1(\theta)P_2(\phi) \tag{4.17}$$

where

$$\int_0^{2\pi}\int_0^{\pi} P(\theta,\phi)\sin\theta d\theta d\phi = 1 \tag{4.18}$$

Since the energy is independent of ϕ, we have

$$\begin{aligned} P_1(\theta) &= \frac{\beta H e^{\beta H \cos\theta}}{2\sinh(\beta H)} \\ P_2(\phi) &= \frac{1}{2\pi} \end{aligned} \tag{4.19}$$

Hence ϕ can be obtained using a random number in the range $[0, 2\pi]$. In order to obtain $X = \cos\theta$ we use the integrated probability $\Pi(X)$

$$\Pi(X) = \int_{-1}^{X} P_1(x)dx \tag{4.20}$$

Since $\Pi(X)$ lies between 0 and 1, we set it equal to a random number r in this range and solve for X

$$X = \cos\theta = 1 + \frac{ln\left[(1-r)e^{-2\beta H} + r\right]}{\beta H} \tag{4.21}$$

Hence we can use two random numbers to obtain a direction of the spin with respect to the field that satisfies the Boltzmann distribution.

However, we must now rotate this local field coordinate system into the fixed global set of coordinates. The transformation is given by

$$\begin{pmatrix} S_x \\ S_y \\ S_z \end{pmatrix} = \begin{pmatrix} \cos\theta_H \cos\phi_H & -\sin\phi_H & \sin\theta_H \cos\phi_H \\ \cos\theta_H \sin\phi_H & \cos\phi_H & \sin\theta_H \sin\phi_H \\ -\sin\theta_H & 0 & \cos\theta_H \end{pmatrix} \begin{pmatrix} S_x\prime \\ S_y\prime \\ S_z\prime \end{pmatrix} \tag{4.22}$$

where the primed coordinates are the field frame and the unprimed coordinates are the global frame.

The Hamiltonian in eqn 4.1 that we will use to study $SrGd_2O_4$ can be rewritten in the form

$$\mathcal{H} = -\sum_i \vec{H}_i.\vec{S}_i \tag{4.23}$$

where $\vec{H}_i$ is the effective field acting on spin i and it includes the exchange field, the dipolar field and any external field. The heat bath algorithm consists of the following steps

1. Select a spin at random and determine the direction of the local field acting on it.

2. Use two random numbers as described above to determine an orientation of the spin with respect to the local field direction.

3. Transform from the local field coordinates to the global coordinates of the entire system

4. Repeat step 1 for all the spins to complete one Monte Carlo step

5. Repeat the entire process many times to calculate the various thermodynamic quantities

The heat bath method has the advantage over the Metropolis method in that there is always a change in spin direction [51].

Since we use a finite sized system for our simulations, it is important to use appropriate boundary conditions to avoid edge effects. In our case we use periodic boundary conditions. For a three dimensional system of length L in each direction the spins $\vec{S}(x, y, z)$ satisfy the following condition:

$$\vec{S}(x, y, x) = \vec{S}(x + L, y, z) = \vec{S}(x, y + L, z) = \vec{S}(x, y, z + L) \tag{4.24}$$

The mean value of a physical quantity Q can be calculated in a Monte Carlo simulation as

$$< Q >= \frac{1}{N} \sum_i Q_i \tag{4.25}$$

where N is the number of Monte Carlo steps and Q_i is the value of Q at each step i. For constant intensive variables such at T and H, the corresponding extensive variables

such as magnetisation and energy fluctuate during the Monte Carlo simulation. The fluctuation in energy is related to the specific heat by the following relation

$$C_v = (\frac{\partial < E >}{\partial T})_T = \frac{< E^2 > - < E >^2}{T^2} \tag{4.26}$$

and the fluctuation in magnetization is related to the susceptibility χ as follows

$$\chi = (\frac{\partial < M >}{\partial H})_T = \frac{< M^2 > - < M >^2}{T} \tag{4.27}$$

Hence we can measure both C_v and χ from the fluctuations in the measured values of E and M about their average values.

4.5 Monte Carlo Errors

For a finite system errors are an inherent property of sampling the states in Monte Carlo simulations. All computers calculate with limited word length and the precession is finite. Statistical and systematic errors are also found in simulations. Statistical errors usually occur due to fluctuations of measured quantities during Monte Carlo sampling. Statistical errors can be estimated by simply taking many measurements of the quantity that we are calculating. On the other hand, systematic errors arise due to the procedure that we use to calculate the thermodynamic quantities. We can minimise systematic errors by checking our codes carefully and testing the algorithms.

The arithmetic average of a quantity Q for R statistically independent observations Q_i can be calculated as

$$\bar{Q} = \frac{1}{R} \sum_{i=1}^{R} Q_i \tag{4.28}$$

For an infinitely large number of observations the probability distribution will be a Gaussian distribution. The statistical error of a quantity Q for a finite system can be estimated by

$$\epsilon = \frac{\sigma(Q)}{\sqrt{R}} \tag{4.29}$$

where the variance $\sigma(Q)$ is the width of the Gaussian distribution.

The fluctuation of a quantity $\delta Q_i = Q_i - \bar{Q}$ is given by

$$\delta\bar{Q}^2 = \frac{1}{R}\sum_{i=1}^{R}(\delta Q_i)^2 = \bar{Q}^2 - (\bar{Q})^2 \tag{4.30}$$

and its expectation value is related to $\sigma(Q)$ as

$$< \delta\bar{Q}^2 >= \sigma^2(1 - \frac{1}{R}) \tag{4.31}$$

Substituting the value of σ into equation 4.29 and using 4.31 we get the statistical error

$$\epsilon = \sqrt{\sum_{1}^{R}(\delta\bar{Q})^2/[R(R-1)]} \tag{4.32}$$

Chapter 5

RESULTS AND DISCUSSION

In this chapter we present the Monte Carlo results obtained for our model Hamiltonian introduced in the previous chapter. Phase transitions are identified from various thermodynamic quantities calculated as a function of temperature and field. The specific heat, the magnetisation and its derivative with respect to field, and the susceptibility are calculated for fields along the three principal axes. These thermodynamic quantities are then used to determine a phase diagram in the $H - T$ plane. In addition to the paramagnetic phase at high T and high H, four separate ordered phases are identified and our results show good agreement with the experimental findings discussed in chapter 3[1]. In the next sections we present our results for the case of pure dipole interactions, pure exchange interactions and both combined. In the simulations we have considered systems with the number of sites $N = L^3$ for $L = 16, 20, 24$ and 28.

5.1 Specific heat

5.1.1 Pure Dipole Interactions

We first consider the specific heat as a function of T in zero applied field in the case of pure dipole interactions. Only the eight nearest neigbours of each site are taken into account. As shown in Fig. 5.1a, the specific heat exhibits one sharp peak at $T \sim 1.05K$. Note that the specific heat calculated from our model Hamiltonian approaches unity (in units of k_B) as $T \to 0$. This is due to the fact that we are using a classical model where the classical spins have two degrees of freedom and the

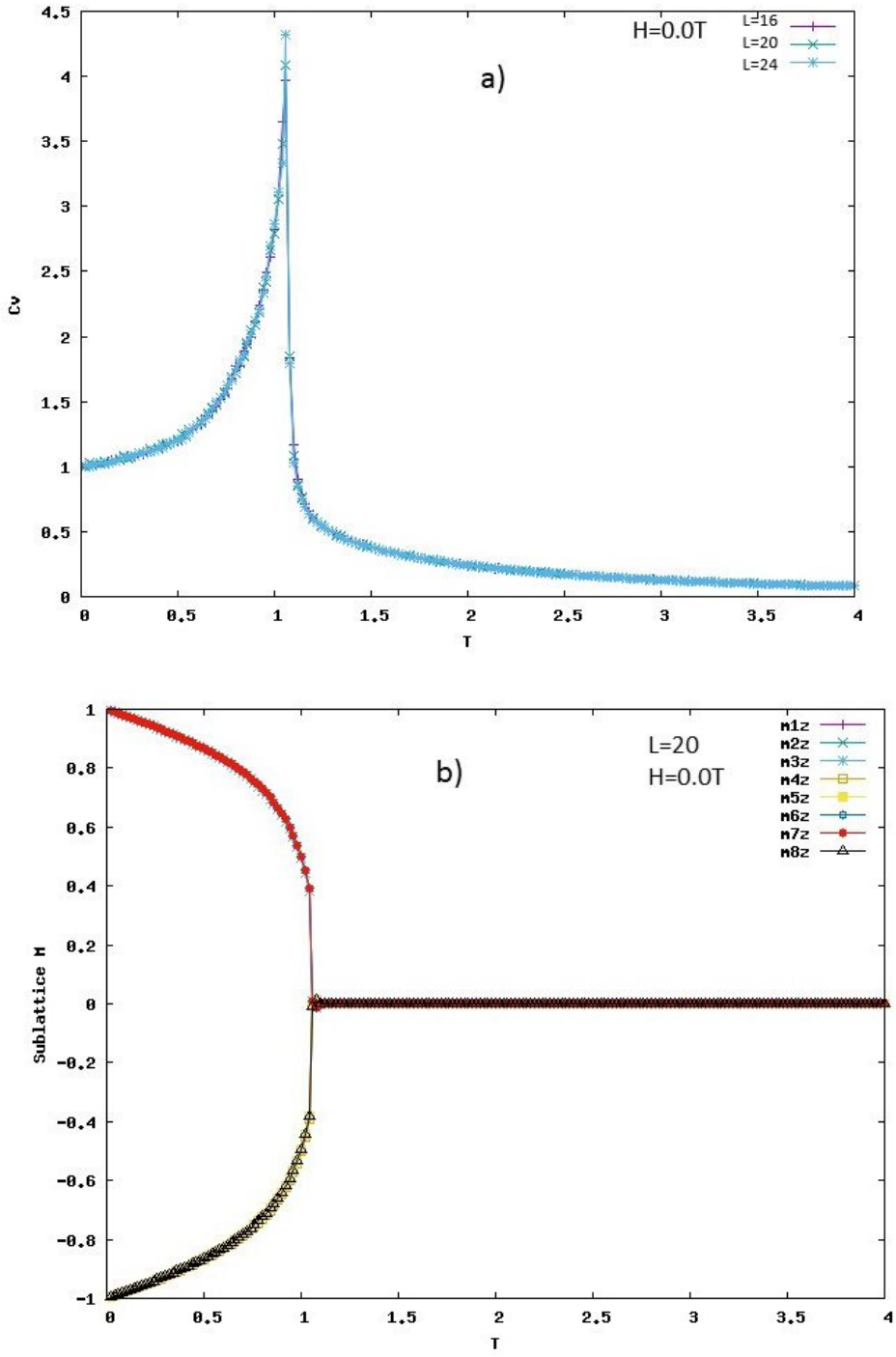

Figure 5.1: a) Specific heat as a function of temperature in zero applied field for pure dipole interactions for lattice sizes $L = 16, 20, 24$. b) Sublattice magnetisations as a function of temperature at zero applied field for pure dipole interactions for $L = 20$.

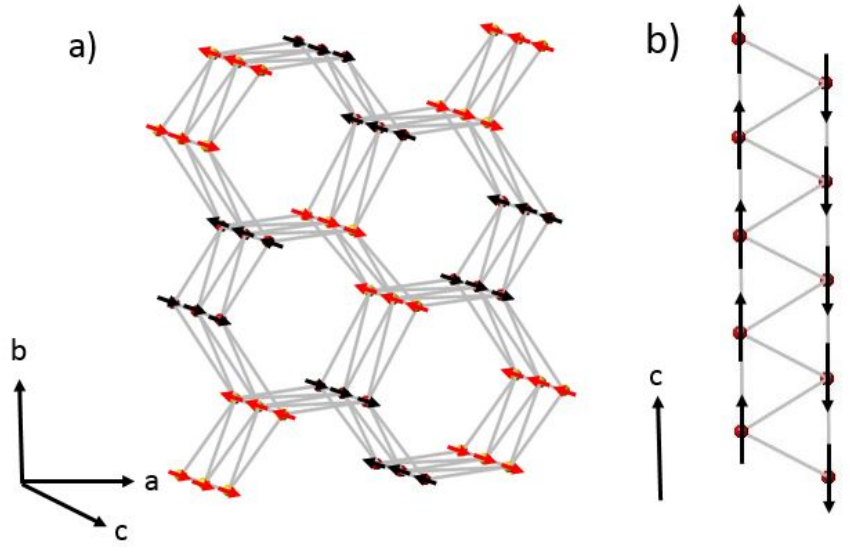

Figure 5.2: a) Ground state configuration in zero applied field for pure dipole interactions. $Gd1$ atoms are indicated in red and $Gd2$ in black. b) Ground state configuration of both the $Gd1$ and $Gd2$ chains.

equipartition theorem can be applied yielding $\frac{1}{2}k_B$ per degree of freedom. The nature of the ordering at $T < 1.05K$ has all spins either up or down along the c axis. Fig. 5.1b shows the z-component of the sublattice magnetisations as a function of T for each of the eight sublattices discussed in Chapter 4. The ground state spin configuration is shown in Fig. 5.2 where it can be seen that the $Gd1$ and $Gd2$ triangular chains along the c direction are all ordered antiferromagnetically. In addition, the chains are arranged such that the directions of the spins alternate from up to down around each hexagon. Thus there is no frustration in this case of pure dipole interactions. The dipole interaction is anisotropic and one expects the c direction to be preferred since the neighbours have the shortest distance in this direction. One would expect that the critical exponents that characterize the transition would belong to the $3D$ Ising model. Indeed the specific heat peak in Fig. 5.1a increases with lattice size L indicating that the specific heat exponent α is positive. However, more precise calculations would be needed to extract the values of the critical exponents.

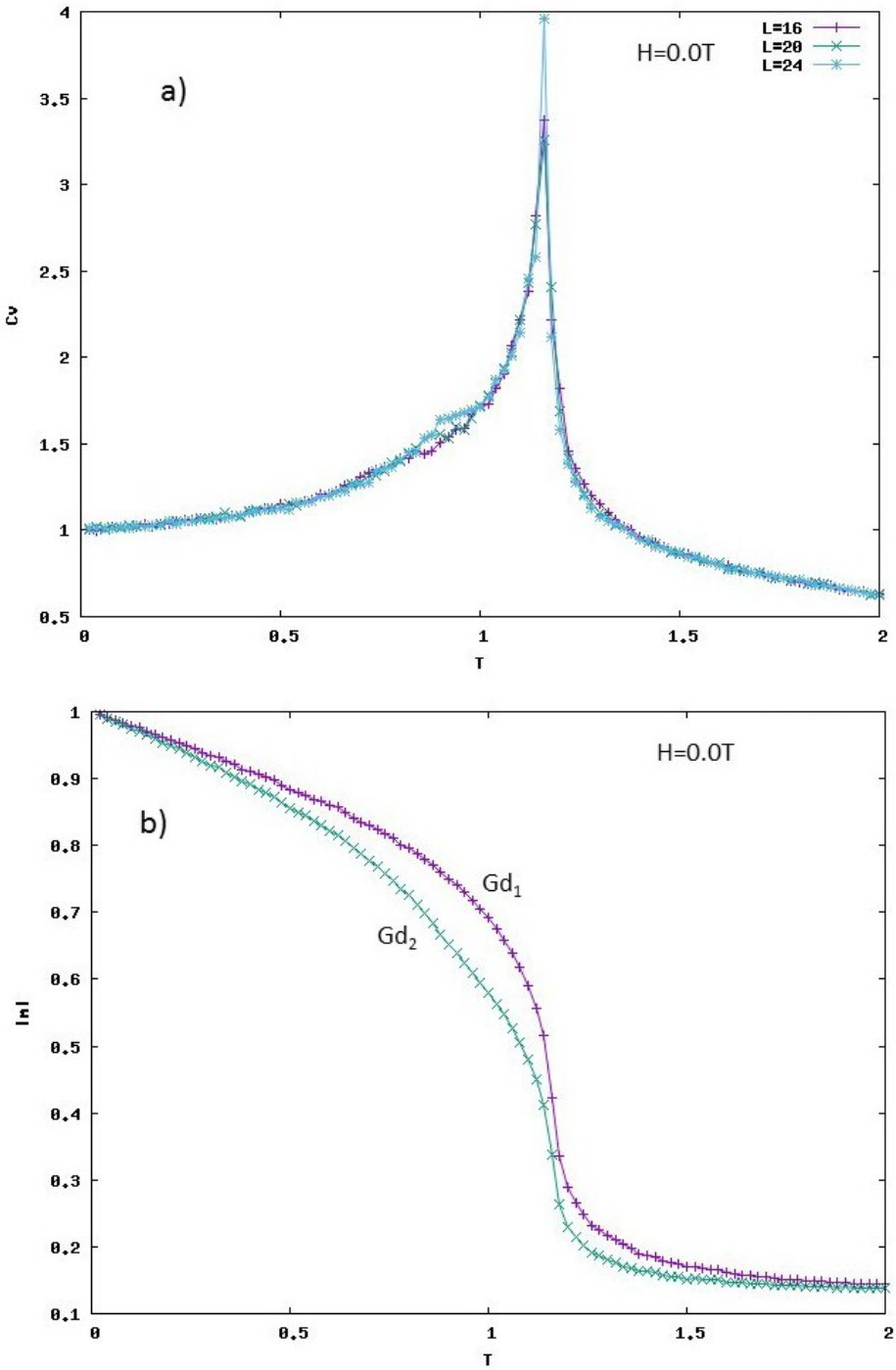

Figure 5.3: a) Specific heat as a function of temperature in zero applied field with only exchange interactions for lattice sizes $L = 16, 20, 24$. b) Magnetisation of a single layer in the c direction of $Gd1$ and $Gd2$ sublattices as a function of T.

5.1.2 Pure Exchange Interactions

The specific heat as a function of T in zero applied field in the case of exchange interactions but no dipole interactions using the exchange parameters tabulated in Table 4.1 is shown in Fig. 5.3a. The specific heat exhibits one sharp peak at $T = 1.15K$ which is very close to the value for pure dipole interactions. There is also an additional bump in the specific heat just below $T = 1K$. In contrast to the situation with only dipole interactions, the nature of the ordering at $T < 1.15K$ is very complex. For each of the sublattices in the unit cell, the spins in each of the layers along the c axis order ferromagnetically but there is no simple relation between the directions of the spins from layer to layer or from sublattice to sublattice. Fig. 5.3b shows the magnitude of the net magnetization in a layer for both the $Gd1$ and $Gd2$ sites as a function of T. All sites order at the same temperature corresponding to the peak in the specific heat but the $Gd1$ and $Gd2$ sites have a different T dependence below the ordering temperature. The $Gd2$ sites have a smaller net magnetisation in each layer and exhibit an almost linear T dependence near $T = 1K$. This behaviour may be related to the additional feature in the specific heat noted above. The magnetisation in each layer is saturated in the ground state but the direction from one layer to the next and from one sublattice to another has no obvious pattern. The system is strongly frustrated. The specific heat peak at $T \sim 1.15K$ does not exhibit a strong dependence on the system size L as in the case of pure dipole interactions. This behaviour is consistent with the $3D$ Heisenberg universality class where $\alpha < 0$.

5.1.3 Exchange and Dipole Interactions

Our results for the specific heat when both exchange and dipole interactions are included are shown in Fig. 5.4a. There are now two sharp peaks in the specific heat at $T \sim 0.63K$ and $T \sim 2.64K$ which agrees qualitatively with the experimental results for $SrGd_2O_4$ previously shown in Fig. 3.10. Fig. 5.4b shows the z component

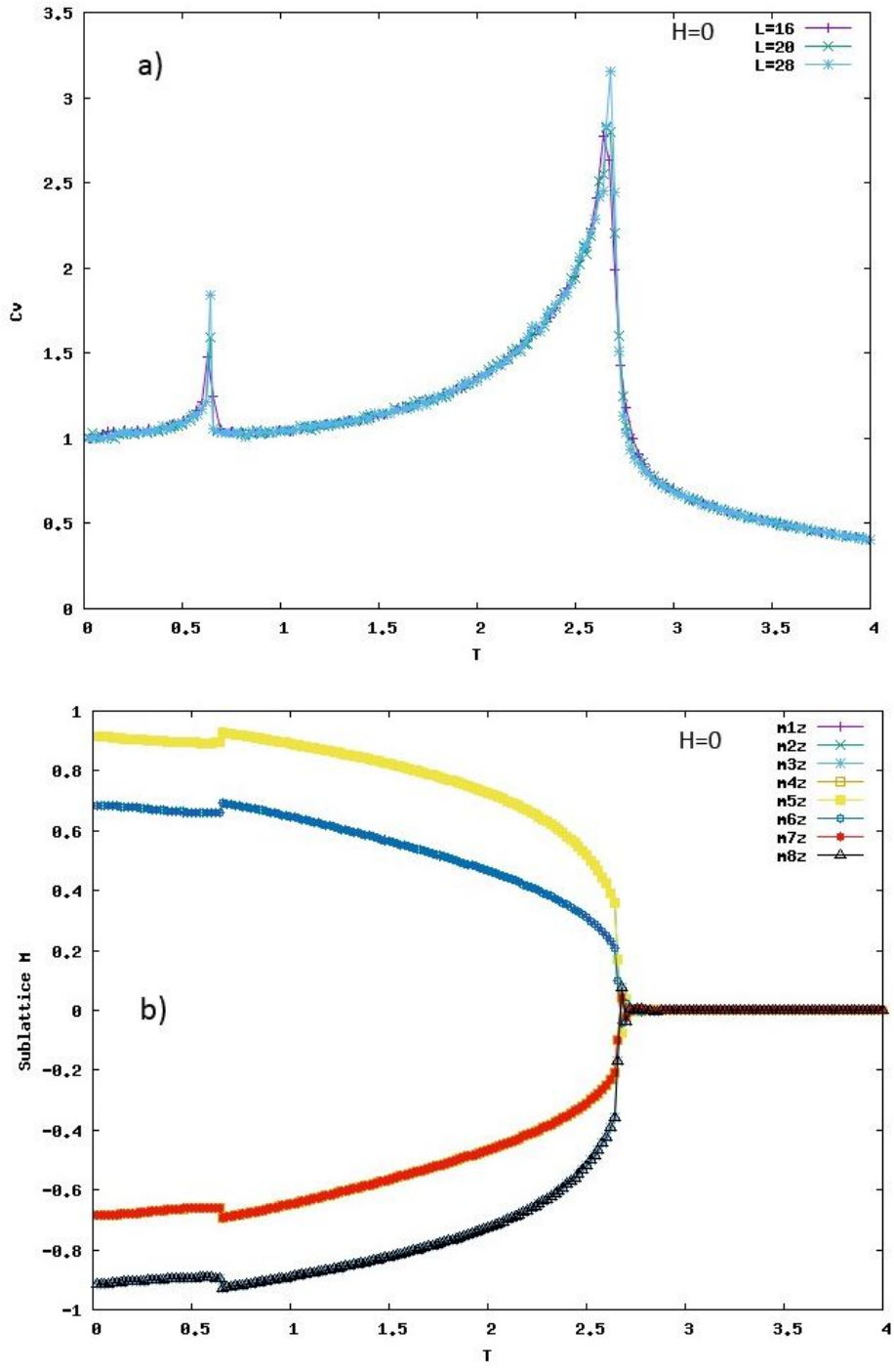

Figure 5.4: a) Specific heat as a function of temperature in zero applied field with both dipole and exchange interactions included for lattice size $L = 16, 20, 28$. b) Sublattice magnetisations as a function of T for $L = 20$ at zero applied field.

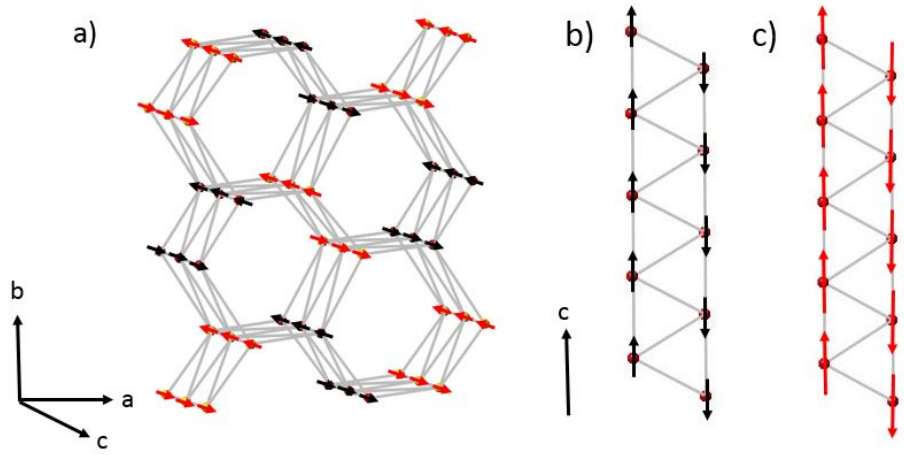

Figure 5.5: Ground state configuration with both exchange and dipole interactions. a) chains are ordered antiferromagnetically but spins have the same orientation along the a direction and opposite orientation along the b direction. b) $Gd2$ chains ordered antiferromagnetically and c) $Gd1$ chains ordered antiferromagnetically but with larger moments.

sublattice magnetisations as a function of T which also exhibit two transitions at the same temperatures as the specific heat. Both the $Gd1$ and $Gd2$ chains have antiferromagnetic order similar to the pure dipole case. However, the magnetisation on the $Gd1$ sublattices is larger than that on the $Gd2$ sublattices. Both show a small decrease at the lower transition and they do not saturate as $T \to 0$. Fig. 5.5 shows the ground state configuration of the spins. Fig. 5.5b and Fig. 5.5c show the antiferromagnetic chains for $Gd2$ and $Gd1$ sites respectively with the $Gd1$ sites having larger magnetisations. The antiferromagnetic chains are arranged differently around the hexagons compared to the pure dipole case in Fig. 5.2a. The spins along the a direction are parallel and the spins along the b direction are anti-parallel.

The competition between the exchange and dipole interactions leads to two phase transitions in zero applied field. In the next subsection we consider the effect of an applied field on the specific heat.

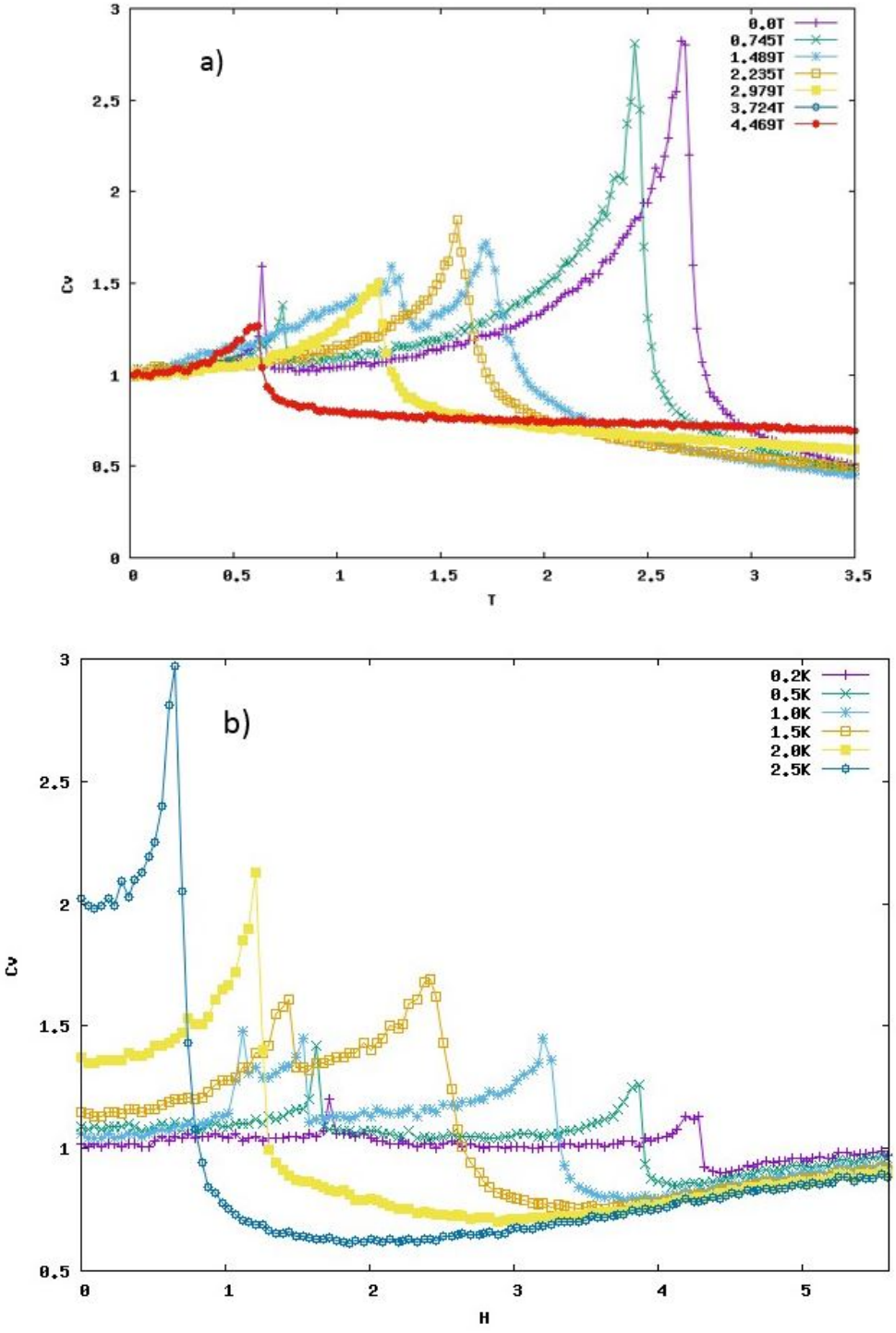

Figure 5.6: a) Specific heat as a function of temperature T at different fixed values of $H \parallel c$. b) Specific heat as a function of field $H \parallel c$ at different fixed values of T.

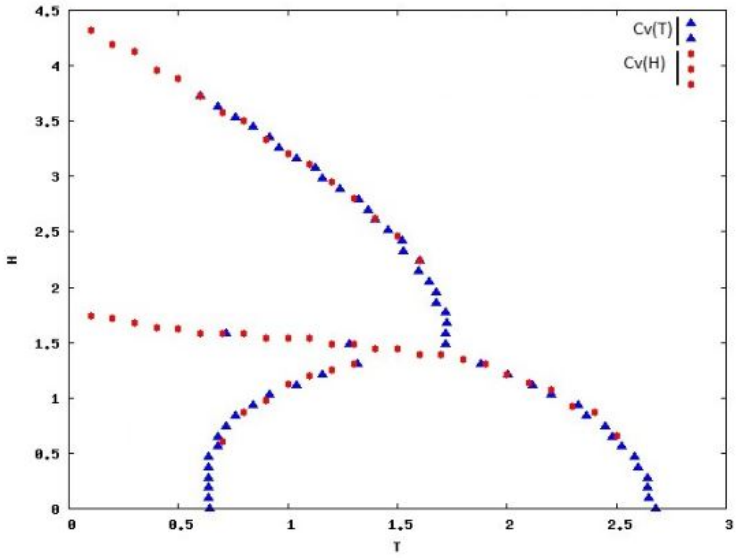

Figure 5.7: Phase diagram based on specific heat data obtained as a function of T at fixed H and as a function of H at fixed T.

5.1.4 Specific Heat in Non-zero Field

Fig. 5.6a shows the specific heat as a function of T at different values of the applied field H applied along the c direction. At low fields two distinct transitions are identified at two different temperatures. However, as the field increases, the peaks shift towards each other and finally merge at $T \sim 1.51K$. For higher fields only one peak remains and shifts towards $T = 0$ near $H = 4.6T$. The field dependent specific heat at different temperatures is shown in figure 5.6b. For fields along c direction the specific heat shows multiple peaks depending on T. At $T = 0.2K$, the data reveals two peaks at two different fields. As the temperature increases there is a small range of T where three peaks are observed which all merge into one peak for $T >\sim 1.7K$.

Using the dependence of the specific heat on both T and H we can construct a phase diagram in the $H-T$ plane as shown in Fig 5.7. In addition to the paramagnetic phase at high T and high H, we identify 3 ordered phases. In order to explore the nature of these phases, we have also studied the total magnetisation and sublattice

magnetisations as a function of field.

5.2 Field Dependent Magnetisation

Fig. 5.8 shows the field dependent magnetisation for applied fields along the three principal axes at $T = 0.5K$. For fields along the a and b directions the magnetisation increases linearly with the field before saturating near $H = 5.0T$. However, for a field along c direction, a sharp jump near $H = 1.6T$ is observed and saturation occurs near $H = 5.0T$. The jump near $H = 1.6T$ is consistent with the phase diagram constructed from the specific heat.

Fig. 5.9 shows the derivative of the z component of the magnetisation with respect to field along the c direction at several fixed values of T. The peaks correspond to jumps in the magnetisation. At $T = 0.1K$ there are peaks near $H \sim 1.8T$ and $H \sim 1.9T$ but for higher $T > 0.4K$ there is only one peak which shifts to lower H as T increases. This behaviour is consistent with the specific heat except at $T < 0.4$ where there appears to be an additional transition. This feature is more evident in the sublattice magnetisations.

Fig. 5.10a shows the sublattice magnetisations as a function of H at $T = 0.2K$. At low fields, there is an antiferromagnetic ordering on all chains which exhibits a spin-flop transition near $H = 1.7T$ followed by a second transition near $2.2T$ where the chains become ferromagnetically ordered reaching saturation close to $H = 4.66T$. Fig 5.10b shows the plot at $T = 1.1K$ where the two low field transitions have merged.

We have also calculated the same sublattice magnetisations as a function of T at a fixed value of H. Fig 5.11a shows the results for $H = 2.235T$ where there is a small bump in the $Gd1$ magnetisation near $T = 1.7K$ and a jump in both the $Gd1$ and $Gd2$ magntisations at $T = 0.2K$. The jumps at the lower temperature indicate the presence of an additional phase compared to the specific heat results. This phase is characterized by ferromagnetic moments on both the $Gd1$ and $Gd2$ chains with two

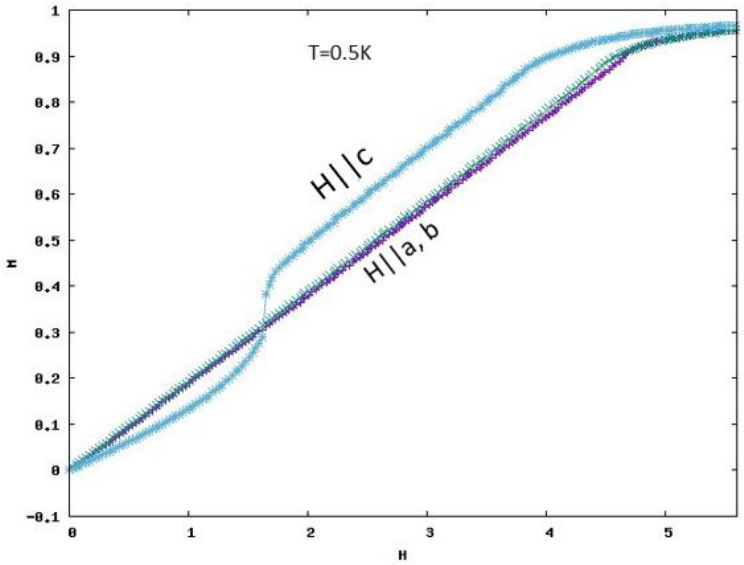

Figure 5.8: Magnetisation vs applied field along three principal directions at temperature T=0.5K. Field along c direction shows a jump at low field.

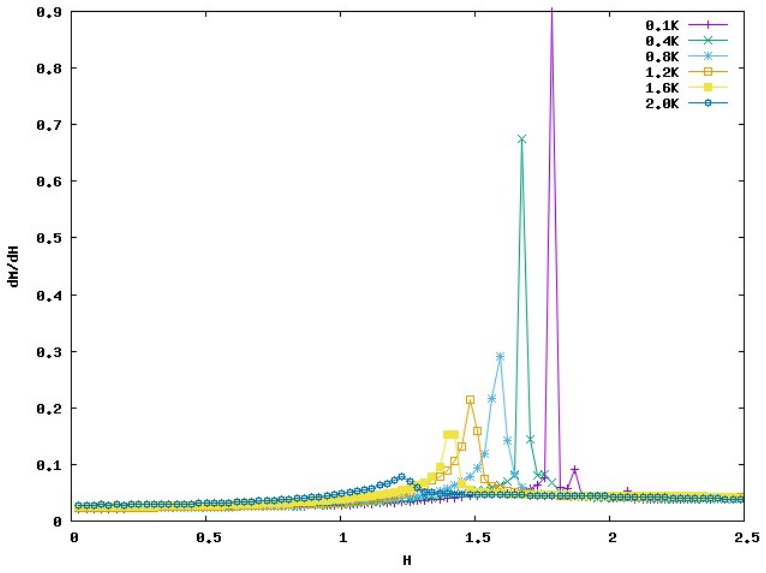

Figure 5.9: Field derivative of magnetisation at various values of T for $H \parallel c$.

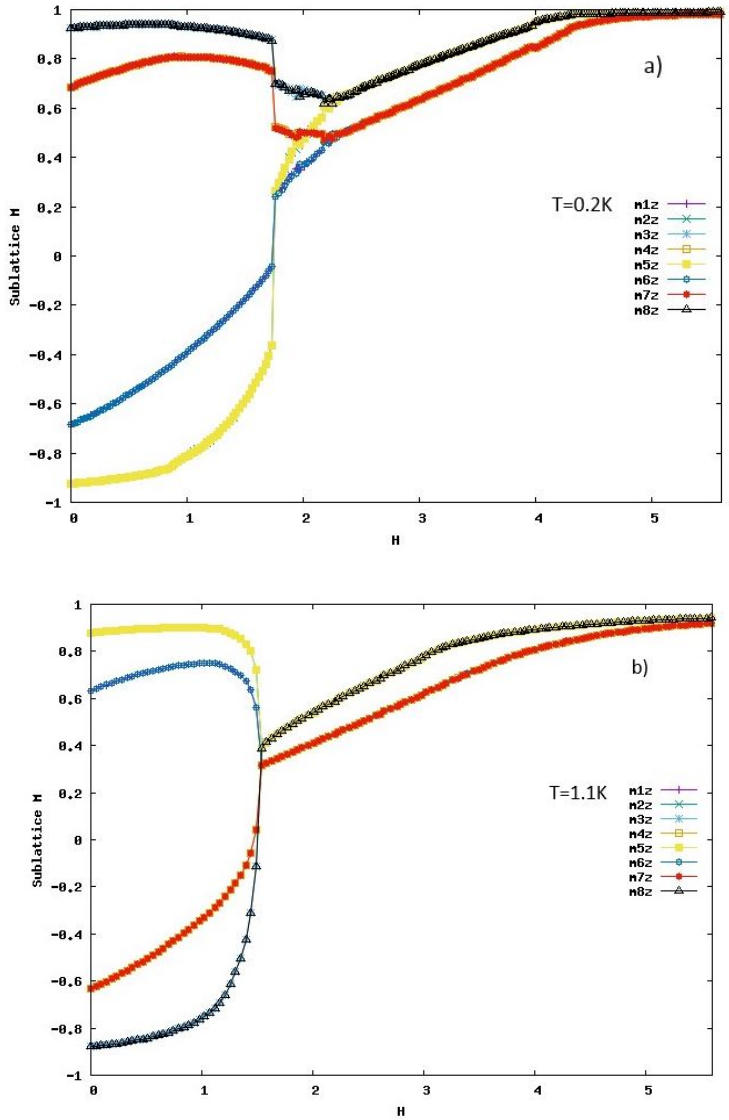

Figure 5.10: a) Sublattice magnetisations as a function of field $H \parallel c$ at temperature $T = 0.2K$. Two transitions at $H = 1.7T$ and $H = 2.2T$ are present. b) Sublattice magnetisations at $T = 1.1K$ where only one transition occurs near $H = 1.5T$.

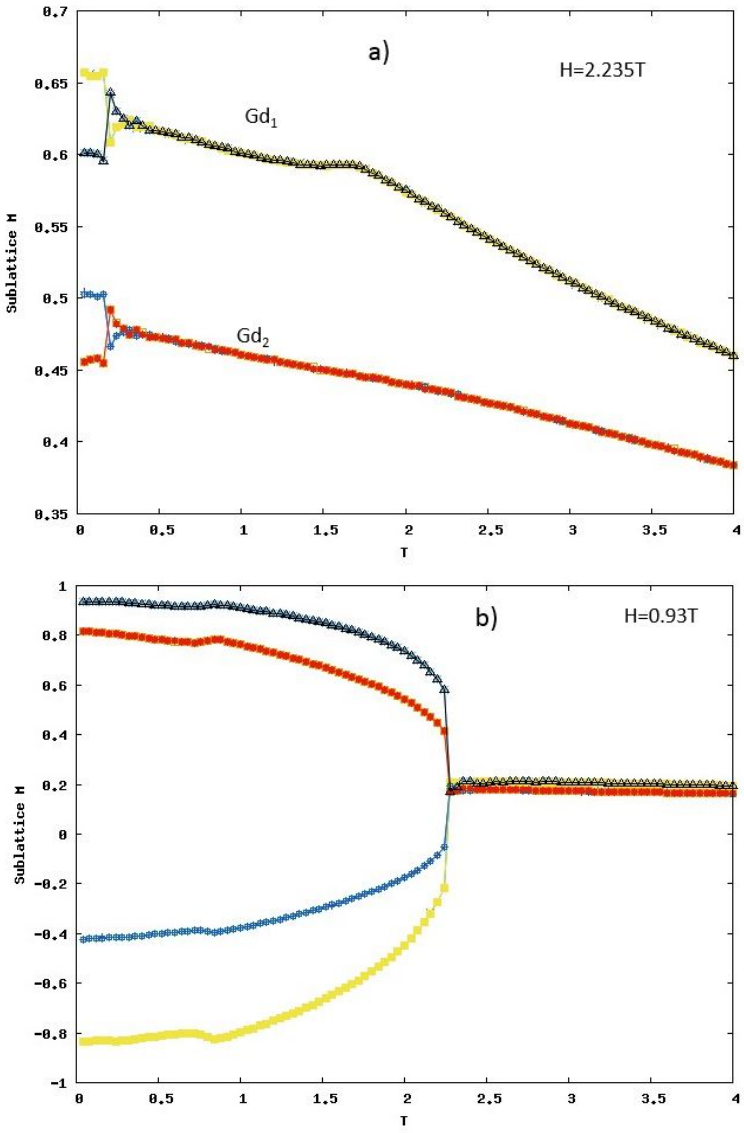

Figure 5.11: a) For applied field $H = 2.235T \parallel c$ sublattice magnetisations as a function of temperature. Near $T = 0.25K$ both chains exhibit a transition ferromagnetic order with two different moments on each chain. At a higher $T \sim 1.5K$ the $Gd1$ sublattice exhibits a peak which signals a transition from the paramagnetic phase to a ferromagnetic phase with the $Gd1$ chains having a larger moment. b) At a lower field of $H = 0.93T \parallel c$, the sublattice magnetisations exhibit a transition to antiferromagnetic order near $T \sim 2.2K$ and an addition small decrease in magnetisation near $T \sim 0.8K$

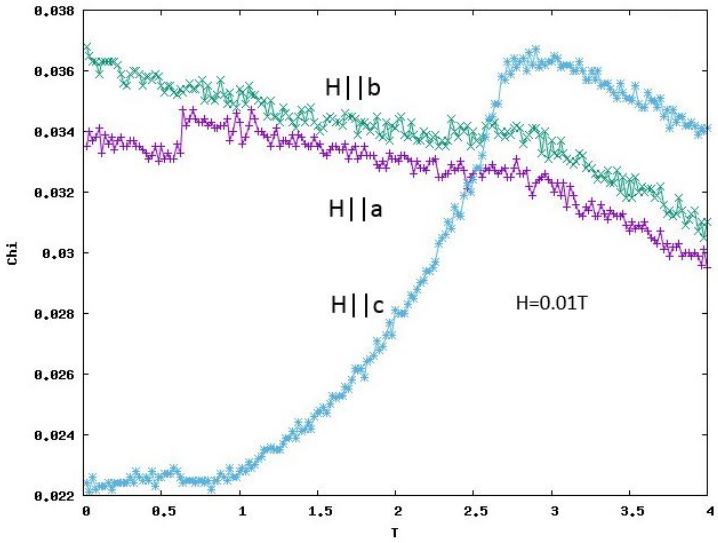

Figure 5.12: Temperature dependent susceptibility for $H = 0.01T$ along the a, b and c directions.

different magnitudes of the moments on the two sides of the chains. Fig. 11b shows the sublattice magnetisations as a function of T at a lower field value of $H = 0.93T$. The results are similar to that previously shown at zero field in Fig. 5.4b. The chains are antiferromagnetically ordered but with a net magnetisation which is larger on the $Gd1$ chains.

5.3 Temperature Dependent Susceptibility

The temperature dependent susceptibilities of the model for a field of $0.01T$ along the three principal axes are shown in figure 5.12. For the a and b directions, the susceptibilities exhibit a small bump at $T \sim 2.7K$. For the c direction there is a cusp at this same temperature which is indicative of antiferromagnetic ordering. In addition, the a and c directions exhibit an upturn near $T \sim 0.6K$ which is similar to the experimental curves in Fig. 3.7. However, the experimental measurements did not extend below $T \sim 0.48K$.

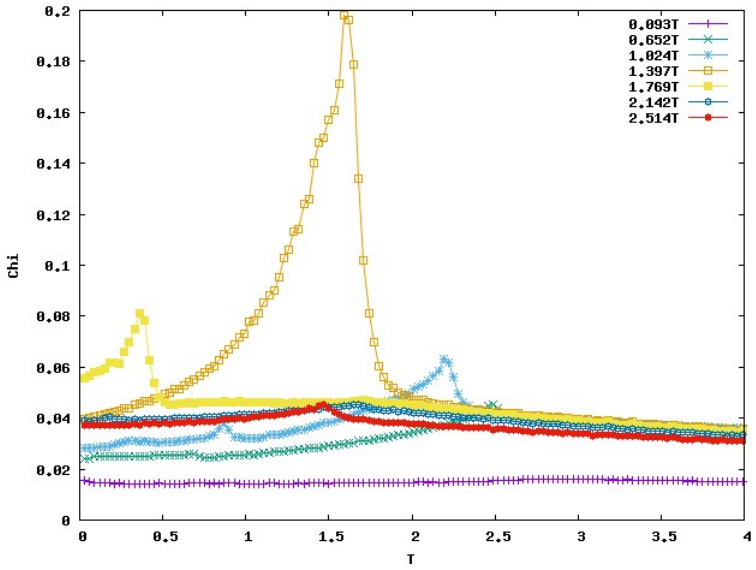

Figure 5.13: Temperature dependent susceptibility as a function of T for several values of $H \parallel c$.

Fig. 5.13 shows the susceptibility as a function of T for several values of $H \parallel c$. As the field increases the high temperature cusp moves down with an additional cusp appearing near $H = 1T$. This is consistent with two anti-ferromagnetic phases. For $H > 1.4T$, a stronger peak in χ appears and shifts to lower T. This latter behaviour is indicative of a ferromagnetic phase.

5.4 H-T Phase Diagram of $SrGd_2O_4$

By collecting all measured thermodynamic quantities(specific heat, magnetisation, susceptibilities) with $H \parallel c$, a magnetic phase diagram is constructed and is shown in figure 5.14.

Magnetic ordering in five phases of the region described above are identified. In region I and II we determined that the magnetic moments are antiferromagnetically ordered. From sublattice magnetisation plots, it seems that there is a subtle difference between these two regions since the sublattice magnetisations decrease as we cross

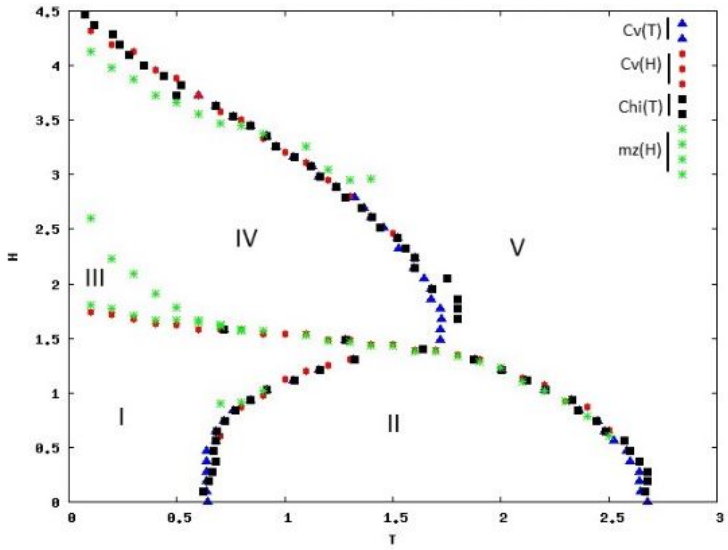

Figure 5.14: H-T phase diagram of $SrGd_2O_4$ from measurements of various thermodynamic quantities, such as specific heat $Cv(T)$, the magnetisation $M(H)$, and the susceptibility $\chi(T)$. Five separate regions represent five types of magnetic ordering.

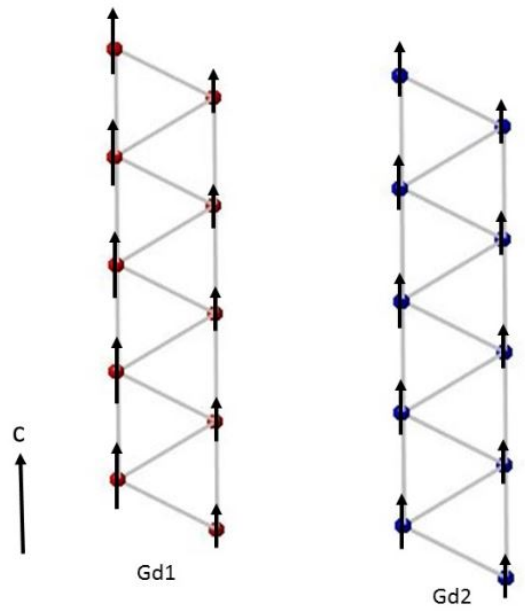

Figure 5.15: Configuration of chains in phase III.

from region II into region I. However in region III, the magnetic orderings are found to be ferromagnetic but with four different sublattice magnetisations as shown in Fig 5.15. Region IV is ferromagnetic but only has two different sublattice magnetisations corresponding to the $Gd1$ and $Gd2$ chains with $Gd1$ chains having a larger value. Region V is the paramagnetic region.

Chapter 6

CONCLUSION

Magnetism studies of the $SrLn_2O_4$ family of compounds have been carred out in the last decade. Two members of the $SrLn_2O_4$ family of compounds($SrGd_2O_4$ and $SrHo_2O_4$) have been studied extensively by Dr. Olga Young[1]. The detailed magnetic properties of $SrGd_2O_4$ obtained from the experimental results have been discussed in chapter 4. For Gd^{3+} ions the orbital angular momentum $L = 0$ and spin-orbit interaction effects are absent and crystal field effects are negligible. Hence this sytem can be modelled using classical Heisenberg spins. In addition to Heisenberg exchange interactions and the Zeeman interaction with an external field, magnetic dipole interactions should the leading perturbation to these terms. We have used Monte Carlo methods to study the phase diagram of $SrGd_2O_4$ using this model. Our simulation results qualitatively agree with the experimental results.

We have studied the specific heat with only dipole interactions and also with only exchange interactions. In both cases, there is only one phase transition in zero applied field. However, when we include both types of interaction, the specific heat exhibits two phase transitions in qualitative agreement with the experiments. Hence dipole-dipole interactions play an important role in this system. The magnetisation as a function of applied field along the three principal directions was also considered. At low T for fields along the a and b directions, the magnetisation increases linearly with no apparent jumps. However, for a field along the c direction, the magnetisation exhibits a jump which signals a spin flop transition. This behaviour is also in qualtitative agreement with the experimental measurements. A $H-T$ phase diagram was constructed using all the measured thermodynamic quantities such as the specific

heat, the magnetisation and sublattice magnetisations with a magnetic field applied along c direction. Clearly five different regions are identified from these measurements. In regions I and II, the triangular chains are ordered in an antiferromagnetic configuration with the $Gd1$ chains having larger moments. At the transition from region I to region II, the moments on both types of chain decrease abruptly but remain anti-ferromagnetically ordered. Ferromagnetic ordering is found in region III with four different moments on the chains. In region IV, each chain is ferromagnetic but the $Gd1$ chains have a larger moment. Region V is the paramagnetic phase where the spins are aligned by the external field with no singular behaviour throughout this region.

The results presented in this thesis are the first simulations of $SrGd_2O_4$. In our calculations, we studied different values of the exchange parameters but those given in Table 4.1 yielded the best agreement with the experimental results. Additional experiments using neutron diffraction could provide detailed information about the ordered phases.

BIBLIOGRAPHY

[1] Olga Young. *Magnetic properties of two geometrically frustrated compounds: $SrHo_2O_4$ and $SrGd_2O_4$*. PhD thesis, University of Warwick, 2013.

[2] Michael Fowler. *Historical beginnings of theories of electricity and magnetism. Recuperado el*, 23(5):2012, 1997.

[3] H A M Snelders. *Oersted's Discovery of Electromagnetism. Romanticism and the Sciences*, pages 228–40, 1990.

[4] Hugh P Vowles. *Early evolution of power engineering. Isis*, 17(2):412–420, 1932.

[5] HT Diep. *Frustrated spin systems*. World Scientific, 2013.

[6] AP Ramirez, GP Espinosa, and AS Cooper. *Strong frustration and dilution-enhanced order in a quasi-2D spin glass. Physical review letters*, 64(17):2070, 1990.

[7] MF Collins and OA Petrenko. *Triangular antiferromagnets. Canadian journal of physics*, 75(9):605–655, 1997.

[8] P Schiffer, AP Ramirez, DA Huse, PL Gammel, U Yaron, DJ Bishop, and AJ Valentino. *Frustration induced spin freezing in a site-ordered magnet: Gadolinium gallium garnet. Physical review letters*, 74(12):2379, 1995.

[9] Oleg Tchernyshyov. *Structural, orbital, and magnetic order in vanadium spinels. Physical review letters*, 93(15):157206, 2004.

[10] Jason S Gardner, Michel JP Gingras, and John E Greedan. *Magnetic pyrochlore oxides. Reviews of modern Physics*, 82(1):53, 2010.

[11] David A Huse and Andrew D Rutenberg. *Classical antiferromagnets on the Kagomé lattice. Physical Review B*, 45(13):7536, 1992.

[12] A B Harris, C Kallin, and A J Berlinsky. *Possible Neel orderings of the Kagome antiferromagnet. Physical Review B*, 45:2899, 1992.

[13] Kurt Binder and A Peter Young. *Spin glasses: Experimental facts, theoretical concepts, and open questions. Reviews of Modern physics*, 58(4):801, 1986.

[14] A Peter Young. *Spin glasses and random fields*, volume 12. World Scientific, 1997.

[15] Roderich Moessner and Arthur P Ramirez. *Geometrical frustration. Phys. Today*, 59(2):24, 2006.

[16] Olga Young, Geetha Balakrishnan, Martin R Lees, and OA Petrenko. *Magnetic properties of geometrically frustrated* $SrGd_2O_4$. *Physical Review B*, 90(9):094421, 2014.

[17] David P Landau and Kurt Binder. *A guide to Monte Carlo simulations in statistical physics*. Cambridge university press, 2014.

[18] David J. Griffiths. *Introduction to Electrodynamics*. Pearson, fourth edition, 2013.

[19] Elmer E. Anderson. *Introduction to Modern physics*. Saunders College Publishing, 1982.

[20] Robert M White. *Quantum theory of magnetism: magnetic properties of materials*, volume 32. Springer Science, 2007.

[21] W. Heisenberg. *Zur theorie des ferromagnetismus. Zeits. fur Physik*, 49:619, 1928.

[22] A.P.M Dirac. *On the theory of Quantum mechanics. Proc. Royal Society*, 112A:661, 1926.

[23] H A Kramers. *L'interaction les atomes magneto genes dans un crystal paramagnetique. Physica*, 1:182, 1934.

[24] PW Anderson. *Antiferromagnetism. Theory of superexchange interaction. Physical Review*, 79(2):350, 1950.

[25] John B. Goodenough. *Theory of the Role of Covalence in the Perovskite-Type Manganites* $[La, M(II)]MnO_3$. *Physical Review*, 100(2):564, 1955.

[26] John B Goodenough. *An Interpretation of the magnetic properties of the perovskite-type mixed crystals. J. Phys. Chem. Solids*, 6:287–297, 1958.

[27] Junjiro Kanamori. *Superexchange interaction and symmetry properties of electron orbitals. Journal of Physics and Chemistry of Solids*, 10(2):87–98, 1959.

[28] David C Johnston. *Magnetic Dipole Interactions in Crystals. Physical Review B*, 93:014421, 2016.

[29] Linus Pauling. *The structure and entropy of ice and of other crystals with some randomness of atomic arrangement. Journal of the American Chemical Society*, 57(12):2680–2684, 1935.

[30] Jacques Villain. *Insulating spin glasses. Zeitschrift für Physik B Condensed Matter*, 33(1):31–42, 1979.

[31] Thomas J. Hayes, Olga Young, Geetha Balakrishnan, and Oleg A. Petrenko. *Magnetisation Studies of Geometrically Frustrated Antiferromagnets $SrLn_2O_4$, with $Ln = Er, Dy$, and Ho. Journal of the Physical Society of Japan*, 81(2):024708, 2012.

[32] H Karunadasa, Q Huang, BG Ueland, JW Lynn, P Schiffer, KA Regan, and RJ Cava. *Honeycombs of triangles and magnetic frustration in SrL_2O_4 (L= Gd, Dy, Ho, Er, Tm, and Yb). Physical Review B*, 71(14):144414, 2005.

[33] AP Ramirez. *Strongly geometrically frustrated magnets. Annual Review of Materials Science*, 24(1):453–480, 1994.

[34] Leon Balents. *Spin liquids in frustrated magnets. Nature*, 464(7286):199–208, 2010.

[35] G Balakrishnan, TJ Hayes, OA Petrenko, and D McK Paul. *High quality single crystals of the SrR_2O_4 family of frustrated magnets. Journal of Physics: Condensed Matter*, 21(1):012202, 2008.

[36] OA Petrenko, Geetha Balakrishnan, Neil R Wilson, S de Brion, E Suard, and LC Chapon. *Low-temperature magnetic ordering in $SrEr_2O_4$. Physical Review B*, 78(18):184410, 2008.

[37] TH Cheffings, Martin R Lees, G Balakrishnan, and OA Petrenko. *Magnetic field-induced ordering in $SrDy_2O_4$. Journal of Physics: Condensed Matter*, 25(25):256001, 2013.

[38] OA Petrenko. *Low-temperature magnetism in the honeycomb systems $SrLn_2O_4$ (Review Article). Low Temperature Physics*, 40(2):106–112, 2014.

[39] OA Petrenko, O Young, D Brunt, G Balakrishnan, P Manuel, DD Khalyavin, and C Ritter. *Evolution of spin correlations in $SrDy_2O_4$ in an applied magnetic field. Physical Review B*, 95(10):104442, 2017.

[40] C Bidaud, O Simard, G Quirion, B Prévost, S Daneau, AD Bianchi, HA Dabkowska, and JA Quilliam. *Dimensionality and irreversibility of field-induced transitions in $SrDy_2O_4$. Physical Review B*, 93(6):060404, 2016.

[41] N Gauthier, A Fennell, B Prévost, A-C Uldry, B Delley, R Sibille, A Désilets-Benoit, HA Dabkowska, GJ Nilsen, L-P Regnault, et al. *Absence of long-range order in the frustrated magnet $SrDy_2O_4$ due to trapped defects from a dimensionality crossover. Physical Review B*, 95(13):134430, 2017.

[42] N Gauthier, A Fennell, B Prevost, A. Desilets-Benoit, H.A. Dabkowska, O. Zaharko, M. Frontzek, R. Sibille, A.D Bianchi, and M. Kenzelmann. *Field dependence of the magnetic correlations of the frustrated magnet $SrDy_2O_4$. Physical Review B*, 95(18):184436, 2017.

[43] Maureen M Julian. *Foundations of Crystallography with Computer Applications*. CRC Press, Taylor and Francis Group, USA, 2015.

[44] A Fennell, VY Pomjakushin, A Uldry, Bernhard Delley, Bobby Prevost, Alexandre Desilets-Benoit, Andrea D Bianchi, Robert I Bewley, Britt R Hansen, Thomasz Klimczuk, et al. *Evidence for $SrHo_2O_4$ and $SrDy_2O_4$ as model J 1-J 2 zigzag chain materials. Physical Review B*, 89(22):224511, 2014.

[45] Olga Young, Andrew R Wildes, P Manuel, B Ouladdiaf, DD Khalyavin, Geetha Balakrishnan, and OA Petrenko. *Highly frustrated magnetism in $SrHo_2O_4$: Co-*

existence of two types of short-range order. Physical Review B, 88(2):024411, 2013.

[46] TJ Hayes, G Balakrishnan, PP Deen, P Manuel, LC Chapon, and OA Petrenko. *Coexistence of the long-range and short-range magnetic order components in* $SrEr_2O_4$. *Physical Review B*, 84(17):174435, 2011.

[47] Paul D. Beale R. K. Pathria. *Statistical Mechanics*. Elsevier Ltd, 2011.

[48] PM Chaikin and T C Lubensky. *Principles of Condensed Matter Physics*. Cambridge University Press, 1995.

[49] N Metroplis, AW Rosenbluth, MN Rosenbluth, and AH Teller. *Equation of state calculations by fast computing machines. J. chem. Phys.*, 21(6):1986–1092, 1953.

[50] Y Miyatake, M Yamamoto, JJ Kim, M Toyonaga, and O Nagai. *On the implementation of the'heat bath'algorithms for Monte Carlo simulations of classical Heisenberg spin systems. Journal of Physics C: Solid State Physics*, 19(14):2539, 1986.

[51] L W Lee and A P Young. *Large-scale Monte Carlo simulations of the isotropic three-dimensional spin glass. Physical Review B*, 76:024405, 2007.